Supporting Information:

# Metallic Nanoislands on Graphene as Highly Sensitive Transducers of Mechanical, Biological, and Optical Signals

Aliaksandr V. Zaretski[1], Samuel E. Root[1], Alexander Savchenko[2,3], Elena Molokanova[4], Adam D. Printz[1], Liban Jibril[1], Gaurav Arya[1], Mark Mercola[2,3], and Darren J. Lipomi[1]*

[1]Department of NanoEngineering, University of California, San Diego, 9500 Gilman Dr., La Jolla, CA 92093-0448

[2]Department of Bioengineering, University of California, San Diego, 9500 Gilman Dr., La Jolla, CA 92093-0412

[3]Sanford-Burnham Medical Research Institute, 10901 N Torrey Pines Rd., La Jolla, CA 92037

[4]NTBS, 309 Hestia Way, Encinitas, CA 92024

*Correspondence to: dlipomi@eng.ucsd.edu

## Graphene synthesis

**Cleaning the copper foil.** Graphene was synthesized on 25-μm-thick copper foils (Alpha Aesar, 13382, 99.8%) with the dimensions of 10 cm × 11 cm. Prior to the growth of graphene, we cleaned the copper foils by soaking them in a shallow acetone bath and wiping them with a Kimwipe tissue (while in acetone). After that the foils were rinsed with acetone and transferred into a similar bath filled with isopropyl alcohol (IPA), mechanical cleaning was repeated in this solvent. We note that the mechanical cleaning resulted in more pristine graphene than after cleaning the foils via sonication in acetone and IPA[1]; this method also saved a considerable amount of the both solvents (considering the large volumes required for sonicating large-area copper foils). After the mechanical cleaning in IPA, the foils were rinsed in IPA and dried in a stream of compressed air.

**Electropolishing the copper foil.** In order to generate mostly single-layer graphene, we found it necessary to electropolish the copper foils prior to graphene synthesis.[1,2] The

clean, dry copper foil was placed into a 250-mL beaker, following the contours of the beaker side-walls, and was used as the anode. A copper pipe ($d$ = 2.54 cm, $l$ = 15 cm) was inserted into the beaker along the cylindrical axis and used as the cathode. The cylindrical shape of the cathode and the curved surface of the anode generated a uniform electric field during the electropolishing. Concentrated phosphoric acid ($H_3PO_4$, 15 M) was used as the electrolyte and was poured into the beaker after the cathode and the anode were secured with a clamp and an alligator clip respectively. A 20 W DC power supply was used to generate the necessary current and voltage. The voltage was set at 1.6 V and electropolishing proceeded until the current fell 50% and plateaued from the initial value (usually between 5 – 10 min). After the electropolishing, the cathode and the electrolyte were removed from the beaker and the copper foil was extensively rinsed with DI water (3 min). Then the copper foil was rinsed with IPA, blow-dried under a stream of compressed air, and immediately loaded into the middle of the quartz tube of a chemical vapor deposition (CVD) reactor.

**Synthesis of graphene.** Atmospheric-pressure CVD graphene synthesis[3] was performed in a quartz tube furnace (MTI OTF-1200X-HVC-UL) with the following tube dimensions: $d$ = 7.6 cm, $l$ = 100 cm. The CVD chamber and the reactor gas-supply lines were purged of air for 5 min by flowing a mixture of all synthesis gases (hydrogen, methane, and argon) at their maximum flow rates while pulling vacuum on the chamber with a diaphragm vacuum pump. After 5 min, the gas flow was stopped and the chamber was evacuated to about $10^{-4}$ torr with a turbomolecular vacuum pump in order to remove methane and hydrogen from the gas-mixing and the reactor chambers as well as to desorb the possible organic contaminants from the surface of the copper foil, then the furnace

was than heated to 730 °C. The chamber was then re-pressurized to atmospheric pressure with ultra-high purity argon (700 SCCM), which flowed constantly throughout the entire procedure of graphene synthesis. The copper foils were heated in argon flow to 1050 °C (30 min). Upon reaching this temperature, additional hydrogen (60 SCCM) was flowed for 60 min to anneal and activate the copper substrate. After the 60 min of annealing, the flow rate of hydrogen was reduced to 5 SCCM. After 30 min, 0.3 SCCM of methane was flowed for 40 min for the synthesis of graphene (total gas flow rate: 700 SCCM argon + 5 SCCM hydrogen + 0.3 SCCM methane = 705.7 SCCM). After 40 min, the flow rate of methane was increased to 0.7 SCCM. After 60 min of total graphene growth time (with methane flow), the furnace was turned off and cracked open 5 cm (continuing the same gas flow). When the furnace cooled to 700 °C (ca. 5 min) it was opened to 10 cm. At 350 °C (ca. 30 min), the furnace was completely opened. At 200 °C, the hydrogen and methane flows were cut off and the reactor chamber was allowed to cool to room temperature in the argon flow (total cooling time was approximately 1 h). The synthesized graphene was analyzed via optical microscopy and a Raman spectromicroscope (**Figure S1**) and was determined to be of high quality and comprising a single-layer with few add-layers. Upon the completion of graphene synthesis, the copper foil bearing graphene was transferred into an oxygen plasma-treated Pyrex dish (to avoid contaminating the graphene with adventitious adsorbents from the ambient air) and evaporation of metal was immediately performed in a cleanroom environment.

**Metal-assisted exfoliation (MAE)**

In order to transfer graphene from copper onto other metals (gold, silver, and nickel), we used metal-assisted exfoliation (MAE) described by us elsewhere.[4] The formation of a

conformal graphene/receiving metal interface in the high vacuum environment during MAE ensures that the interface is free from oxides and other contaminants and that the resultant morphologies after the subsequent nanoisland deposition are solely a function of the materials involved and the processing parameters.

**Deposition of metal and self-assembly of nanoisland (NI) films**

To compare the NI morphologies resulting from the selection of the underlying substrate, we used a Temescal BJD-1800 e-beam evaporator to deposit 10 nm of evaporant (gold or silver) onto graphene supported by copper, nickel, gold, and silver. The graphene-bearing substrates were fixed to the sample stage and positioned directly under the source of the evaporant (at distance of 40 cm). The metal evaporation rate was kept low (0.1 Å $s^{-1}$, as monitored by a quartz crystal microbalance) and the chamber pressure was kept at $7 \times 10^{-7}$ torr during evaporation. The temperature of the substrate at the end of the evaporation was 400 K (further in text referred to as standard deposition conditions - SDC). The rate of evaporation and the temperature of the substrate are important parameters that determine the resulting morphology of the NI. We performed control evaporations of 10 nm of gold onto graphene supported by copper at 2 Å/s, 400 K and at 0.1 Å/s, 500 K. We have found that even though graphene offers very low diffusion barriers for gold and silver atoms, the faster rate of evaporation (2 Å/s as opposed to 0.1 Å/s) biases the process to be more kinetically-controlled and results in a less-structured morphology (**Figure S4**). Conversely, higher temperatures (500 K as opposed to 400 K) result in morphologies of higher crystallinity and lower area coverage (**Figure S5**).[5]

All samples were analyzed using the XL30 FEI SFEG UHR scanning electron microscope (SEM). By SEM imaging we have determined that the morphology on the

NI depends on the crystallographic orientation of the underlying substrate. **Figure S2** demonstrates the difference in morphology of AgNI resulting from deposition of 10 nm of silver onto graphene on copper substrate (at SDC) with two neighboring copper grains of different orientations. In order to determine if the number of graphene layers between the substrate and the evaporant influence the NI self-assembly, we deposited 10 nm of gold at SDC onto copper substrate bearing graphene with a greater density of ad-layers. Further, the copper/graphene/AuNI were coated with 1 μm of Parylene C using a PDS 2010 Parylene coater. Upon etching of the underlying copper, the Parylene/AuNI/graphene was imaged using the SEM (the AuNI were imaged through the underlying graphene). In **Figure S3** it is seen that the amount of percolation on the AuNI decreased on graphene bearing progressively more layers. This correlated well with the model for thin-film growth, since additional graphene layers sequentially lowered the surface energy of copper.[6]

We would like to note the repeatability of the AuNI morphology between samples for which depositions were performed at similar conditions (film thickness, rate of deposition, chamber pressure and temperature) and on similarly synthesized graphene (AuNI on copper in **Figures 1** and **S22**). In **Figure S22** it is seen that the AuNI morphology is consistent over the entire graphene sample of as large as 40 $cm^2$ in area. From this we conclude that the methodology described in this letter is applicable to large area substrates and is possibly limited in scale by the dimensions of the equipment utilized.

**Transfer of graphene/NI films**

For many applications, NI have to be transferred from the substrate upon which they were generated onto the final receiving substrate (optical fiber, glass slide, PDMS, PET, human skin, etc.). The transfer to glass coverslips, silicon wafers and strips of PDMS was performed following the well-established methodology for transferring graphene.[7] First, the supporting layer of PMMA (100 nm thick) was spin-coated onto copper/graphene/NI, followed by etching of the copper substrate in 1M iron (III) chloride (FeCl3) for 1 hour. After this, the graphene/NI/PMMA film was free floating on the surface of the etchant and was scooped and transferred into a beaker containing deionized water (3 times, 5 min in each beaker) in order to remove contaminants residual from etching the copper. The graphene/NI/PMMA was then scooped with a piece of a silicon wafer for SEM analysis, (**Figure S7**). Strikingly, the morphology of the graphene/AuNI as transferred to the silicon wafer was very different than that before the transfer (**Figure 1**). The AuNI formed a completely percolated network and lost sharp crystal edges and corners in favor of rounded features. This effect is likely due to substituting (intermittently) the substrate with a high surface area (copper, 1650 $mJ/m^2$) from under graphene/AuNI for water with a low surface energy (72 mJ/m2). The stabilizing substrate crystallinity also disappears with etching of the copper. At this stage, the AuNI apparently reconstruct into the most thermodynamically favorable configuration and likely retain it upon their placement onto the final receiving substrate. Note that this drastic reconstruction occurs in STP conditions. A free-floating film consisting of graphene/NI/polymer (**Figure S16**) can be deposited onto a substrate in one of two ways: the final receiving substrate interfacing with the graphene or conversely with the supporting polymer. In the first case, the substrate has to first be submerged into the DI water and slowly lifted out of the water

picking up the floating composite film in a Langmuir-Blodgett fashion (optical fibers, glass coverslips and PDMS strips were coated in this way for Raman sensing, rigid substrate and flexible substrate strain sensing respectively). In the second case, the substrate is plunged into the floating graphene/NI/polymer film and further down into the water (**Figure S17**) (substrates for cardiomyocyte culture and contraction experiments and well as heart-rate monitoring were coated in this way). If sensors are supported by PMMA during transfer, this supporting polymer film can be easily removed with acetone. Noticeably, no supporting polymer was used for coating the tips of optical fibers with graphene/AuNI films, as the area of a tip (~0.03 $mm^2$) is significantly smaller than the fragments resulting from breakage of the unsupported graphene/NI film (when such breakage occurs).

In addition to the abovementioned transfer methods, a polymeric film can be laminated on top of the copper/graphene/NI film (e.g. with a commercial laminator) and thus serve as the supporting and final receiving substrate upon copper etching.[8] Such transfer was used by us to generate flexible strain sensors supported by 125 μm-thick polyethylterephtalate (PET) (**Figure S18c,d**).

**Atomistic Physical Vapor Deposition Simulations**

All simulations were performed using the open-source simulation package LAMMPS (12/09/2014)[9] as available on the Comet supercomputer at the San Diego Supercomputer Center. The simulations were accelerated with a dynamically load-balanced domain decomposition using a message-passing interface distributed on two compute nodes containing a total of 48 Intel Xeon processors. We achieved a parallel speed up of ~20× corresponding to an efficiency of ~ 5 ns/day. Visualization and post-processing analyses

were performed using the open-sourced visualization tool, OVITO[10] along with a custom python module.

The initial configuration of the graphene/copper (111) surface was generated and equilibrated following the procedure of Süle et al.[11] Specifically, we chose to use a 3 × 3 Moiré super cell[12,13] with a thick copper support (30 layers) and fixed its bottommost layer to effectively model a bulk copper surface. A vacuum layer of height of 4 nm was inserted above the surface to deposit the gold atoms and provide space for the islands to grow. A reflective boundary condition was imposed in the vertical direction with periodic boundaries in the horizontal directions. A schematic of the initial simulation cell is provided in **Figure S21**.

**Simulated gold deposition.** To simulate the deposition process, gold atoms were introduced at random positions within the insertion plane of the vacuum region at a rate of 200 particles per ns with a velocity directed at the surface. This deposition rate was chosen due to computational constraints. Although it is orders of magnitude larger than the experimental rate, it is the best we can do to perform these simulations in a reasonable amount of time and is standard practice throughout the literature.[14,15] The particle velocities were sampled from the Maxwell-Boltzmann distribution at a temperature commensurate with the experimental evaporation temperature. The temperature of the entire system was maintained at 400 K throughout the deposition process using a Nosé-Hoover style thermostat[16] in an NVT ensemble with a time constant of 0.01 ps. The equations of motion were integrated with a time-reversible, measure preserving Verlet algorithm[17] using a time step of 1 femtosecond, which was found to result in numerically stable simulations.

**Simulation of thermal annealing.** Following the deposition process, the experimental vacuum annealing process was simulated by increasing the temperature to 500 K and allowing the gold islands to diffuse and aggregate until the morphology became stable (~15 ns). During annealing, the surface area of the gold clusters was monitored using the surface mesh modification[18] from the OVITO software package with probe sphere radius of 2.5 Å and a smoothing level of 20.

**Interatomic Potentials.** Due to the hybrid nature of the system, each pair-wise interaction was treated independently with an appropriate interatomic potential. The metal-metal interactions were all computed using the embedded-atom method, which has been extensively used and verified throughout the literature for metallic systems.[19] The carbon-carbon interactions were treated using an AIREBO potential,[20] which has been shown to be a good model for graphene[11]. Carbon-copper interactions were treated using an angle-dependent Abell-Tersoff potential[21], which was parameterized specifically for this system using high level density-functional theory calculations[11]. Finally, the carbon-gold interactions were treated using a Lennard-Jones potential (epsilon = 0.0341 eV, sigma = 3.003 angstrom),[22] which has been shown to provide an accurate description of the binding and diffusion of gold on graphene, so long as there are no defects or grain boundaries present (which is the case in this study). A summary of the interatomic potentials used can be seen in **Table S21**.

**Statistical Analysis of Island Growth.** The trajectory files output from the physical vapor deposition simulations provide a wealth of information that can be used to quantitatively characterize the morphological evolution and growth of the nanoislands. These metrics provide a basis for comparing different systems and can give insights into

the physical mechanisms underlying island growth unattainable from experiments alone. One quantity that can be quite easily monitored is the coordination numbers of the individual gold atoms. To calculate this we used a custom python code to parse through snapshots of the trajectory file and calculate all the nearest neighbors for every gold particle using the bond length as a distance cutoff. **Figure S19** shows the evolution of the probability distribution of the coordination number of the gold particles as the islands grow. From these results, we see that after 0.5 nm of Au has been deposited the majority of the gold atoms have a coordination number of 6, which corresponds to the surface of the cluster. After 1 nm has been deposited, we see that the majority of the gold atoms have a coordination number of 12, which corresponds to the bulk of the clusters.

Another quantitative metric to characterize the gold island growth is the distribution of the heights of the gold particles. These were calculated by binning the gold particles from a trajectory snapshot with respect to their vertical heights and normalizing the distribution. **Figure S10** shows the evolution of this probability distribution during the deposition process. We can see that with only 0.5 nm Au deposited, we have a maximum island height of 6 layers (22 Å). This result clearly demonstrates the preference of the gold clusters to bunch up instead of spreading out over the surface, likely due to more favorable gold/gold interactions versus gold/substrate interactions. We will use the above analysis to compare the effect of underlying substrate and deposited metal on island growth in future computational experiments.

**Optical fiber Raman sensors**

In order to study the feasibility of using the graphene/NI composite films as SERS substrates for label-free sensing, we transferred unsupported graphene/AuNI onto tips of

freshly cleaved 300 µm-thick optical fibers (core: 50 µm in diameter, 50 µm-thick cladding, 50 µm-thick sheath). 7.5 nm of gold was evaporated onto graphene on copper in order to obtain non-percolated AuNI with minimal gaps between them (**Figure 3b, right inset**) (we have established 7.5-8 nm of Au deposition to be the percolation threshold for AuNI). After transferring the films and drying the fibers overnight in ambient air, they were placed into a beaker containing a 10 mM ethanolic solution of 1-butanethiol (BT) together with a 1 $cm^2$ piece of a silicon wafer with an evaporated 100 nm-thick film of gold (as a control substrate) in order to form a self-assembled monolayer (SAM) of BT on gold surfaces. After 24 h, the test substrates were thoroughly rinsed in DI water and isopropanol (IPA) and dried in ambient air.

**Raman spectroscopy analysis.** For obtaining the Raman spectra from the test substrates, a Raman microscope (Renishaw inVia) with an inverted stage and with a 785 nm excitation source was used. For both test samples and the control, the laser beam was focused to a 2 µm beam spot and the exposure was set to 60 seconds at 0.5 mW power. It is worthy to note that we were able to obtain distinct BT signals from the tips of the coated optical fibers (albeit with a low signal-to-noise ratio) even at as low as one second exposure, while no BT signal was obtainable at 60 s exposure even by raising the beam power to 5 and then to 50 mW. This indicates that graphene/AuNI are suitable SERS substrates and far superior to unstructured gold films.

**Graphene/PdNI films as strain sensors**

We have noticed that depositing ~10 nm of Pd onto graphene on copper under the SDC resulted in formation of a uniform monolayer of spherical particles (4-5 nm in diameter). We further transferred these graphene/PdNI onto rigid (glass), flexible (PET) and

stretchable (PDMS) substrates (**Figure S18**) in order to test their piezoresistive properties over large range of strains.

**PdNI sensors on rigid substrates.** In order to evaluate the performance of PdNI as strain sensors under very low strains <<1%, 3-5 by 25 mm graphene/PdNI/PMMA strips were transferred onto 1 in × 1 in glass coverslips that were 130 μm thick. To remove PMMA, the slides were rinsed with acetone. To electrically address the sensor, copper wires (36 gauge) were adhered to the PdNI and glass coverslips with copper tape bearing conductive adhesive and drops of EGaIn were placed on the loose wire ends to ensure a stable electrical contact (**Figure S18a**). In all cases the aspect ratio of PdNI sensors after the attachment of electrodes was between 3 and 10 and unstrained resistance between 644 and 2015 Ohms.

To induce and register very small strains (0.001%-0.003%) with PdNI sensors, we placed 13 μm-thick polyimide (PI) tape (1 layer for 0.001% and 3 layers for 0.003% strain) onto a 2 in × 3 in glass slide. We then used the PI as a step of controllable height to create a cantilever by resting and fixing one half of the PdNI-coated glass coverslip on the tape while creating a gap between the coverslip and the glass slide under the other half of the coverslip (**Figure 3f**). By applying a small force (~0.1 N) to the free end of the cantilever and bringing it in contact with the glass slide, we bent the glass slide inducing tensile strains on its PdNI-coated surface and registered the resistance change with a Keithley 2400 source/meter using a custom-generated LabVIEW code (**Figure 3f, right inset**). Solid Pd film control samples were analyzed in a similar fashion (**Figure S15**).

**PdNI sensors on stretchable substrates.** To measure the piezoresistivity of PdNI sensors at higher strains (>1%), we transferred them onto strips of PDMS (3 mm × 10

mm × 100 mm), addressed them with copper wires and EGaIn, and used a high-precision linear actuator to stretch the PDMS (**Figure S18b**). Graphene (without PdNI) control samples were analyzed in a similar fashion. We cycled the sensors between 0% and 9% with 1% intervals (20 cycles per each 1% interval) (**Figure 3e**). The sensors exhibited very high gauge factors and cyclability while maintaining a stable baseline (**Figure S20**).

**Heart rate measurements.** In order to obtain biometric signals, we spincoated 8 μm-thick PDMS films on copper/graphene/PdNI, cured the PDMS on a hotplate at 100 °C for 10 min, and etched the copper in 1 M iron (III) chloride (1 h). Then we transferred the free-floating graphene/PdNI/PDMS films into DI water (3 times) and deposited the sensor onto the skin on the wrist (on top of the radial artery) (**Figure 3d**) by plunging the wrist into the vessel with the DI water and the sensor. The PDMS surface formed a good interface with the skin. Previously to depositing the sensor, we adhered a strip of an adhesive tape around the wrist while leaving a section of the skin above the radial artery tape-free. The adhesive tape served two purposes: it helped the attachment and keeping in place of the electrical contact wires and localized the strain on the tape-free section of the skin by rendering the tape-covered skin unstretchable. It is worthy to note that out of three sensors prepared this way, only one sensor was able to measure the heartrate while the other sensors generated wrinkles in PDMS during the transfer process and were not sensitive enough (although all three sensors were able to register wrist and individual digit motions with a high fidelity).

**In-situ SEM on PdNI sensors**. In order to register the film morphology of PdNI sensors under 0.001%, 3%, and 5% strains, we imaged them with the XL30 FEI SFEG UHR scanning electron microscope. To image the sensors under small strains on the rigid

substrate, the PI tape step methodology was used. Here, instead of applying intermittent force on the cantilever, we permanently taped the free end of the cantilever to the glass slide with a conductive copper tape. This tape also served as an electrical ground electrode to discharge the sample to the SEM stage.

For obtaining the images of the sensor films under 3% and 5% strain, the sensors supported by 1 mm-thick PDMS strips were adhered to the curved surfaces of 3D-printed half-cylinders with the radii of curvature of 15mm and 10mm respectively (bending PDMS strips to the specified radii generated surface tensile strains of 3 and 5%) by using the adherent copper tape that also served to electrically ground the samples to the SEM stage.

**Application-specific NI.** We would like to point out the universality of the suggested platform in generating substrates for various applications. The selection of the optimal morphology and materials depends entirely on the application. Thus for a cellular biology sensing application, biocompatibility is potentially the greatest concern, so the metals are mostly limited to gold. This material limitation is also the case with the SERS sensing applications, where the metal has to be plasmonically active in the desired spectrum. Additional desired morphological traits for SERS sensing are morphologies with sharp features (plasmonic hot spots) and small gaps (ideally 1-3 nm). We believe that the ideal morphologies for strain sensors are those that would support the tunneling current piezoresistivity (for sensing extremely low strains) while providing the maximum coverage of the graphene area in order to “heal” the cracks generated by higher strains upon relaxation. For this reason, for strain sensing we found palladium NI to outperform the films bearing other morphologies.

**Electrophysiology**

Neonatal rat ventricular cardiomyocytes were isolated using the neonatal rat cardiomyocyte isolation kit (Worthington) and cultured at 37 °C with 5% $CO_2$. In brief, ventricles were dissected from 1-day-old Hsd:SD rats (Sprague Dawley), then digested overnight at 4 °C with trypsin. Digestion continued the following morning with collagenase for approximately 60 min at 37 °C. Cells were pre-plated for 90 min to remove fibroblasts, and plated on 12 mm glass coverslips coated with PMMA/AuNI/graphene in high-serum media (DMEM/F12 [1:1], 0.2% BSA, 3 mM sodium-pyruvate, 0.1 mM ascorbic acid, 4 mg/liter transferrin, 2 mM L-glutamine, 100 nM thyroid hormone (T3) supplemented with 10% horse serum and 5% fetal bovine serum) at $2 \times 10^5$ cells/cm$^2$. After 24 h, media was changed to low-serum medium (same as above but with only 0.25% fetal bovine serum). Three cell cultures were plated on PMMA/AuNI/graphene with at least 8 substrates in each cell culture. We coated several PMMA/AuNI/graphene substrates with Matrigel in each cell culture plating in order to compare the adhesion of cells to bare PMMA/AuNI/graphene substrates and those coated with Matrigel. We noticed no difference in cell adhesion and viability between the samples.

**Scanning Electron Microscopy**. First, cells were washed with 0.1 M phosphate buffer (pH 7.4), then fixed with 4% formaldehyde solution for 2 hours at room temperature, and washed with the same buffer three times for 5 min each. Following dehydration with graded series of alcohol (30% ethanol – 10 min, 50% ethanol - 10 min, 70% ethanol - 10 min, 80% ethanol - 10 min, 95% ethanol – 2 changes in 10 min, 100% ethanol – 3 changes in 15 min), all samples were freeze dried in a vacuum chamber, and coated with

sputtered iridium. Scanning electron microscopy images were acquired on the XL30 FEI SFEG UHR at the working distance of 5 mm while using the 10 kV energy beam.

**Electrophysiological measurements**. A custom electrophysiology chamber was built by 3D printing a mold in which PDMS (Sylgard 184) was cured. The finished chamber had a central opening (for cell culture and media) and side openings (for eutectic electrode placement) and was placed on top of the glass coverslips bearing PMMA/AuNI/graphene and CM culture in a way that the central portion of the AuNI substrate was located in the central opening and the edges of the AuNI substrate were accessible for electrical addressing using EGaIn through the side openings (**Figure 4a**). The assembly was then sandwiched between two 1 in × 3 in glass slides and clamped with binder clips to ensure a good seal. A 5 mm aperture was pre-drilled in the top glass slide to allow adding media to the central opening of the chamber. The PDMS walls between the camber openings served to separate the EGaIn electrodes from the cell media (in mM, NaCl, 135; KCl, 2.5; $CaCl_2$, 2; $NaHCO_3$, 1; $Na_2HPO_4$, 0.34; $KH_2PO_4$, 0.44; glucose, 20; and HEPES, 10 (pH 7.4). Electrophysiological recordings were performed in current-clamp configuration using a Digidata 1322 interface, an Axopatch 200B amplifier, and pClamp software (Molecular Devices Corp.). The data were digitally sampled at 50 kHz and filtered at 2 kHz. Experiments were performed at room temperature. All traces representing individual contractions were fitted with exponential functions using Clampfit10.3 and OriginPro2015.

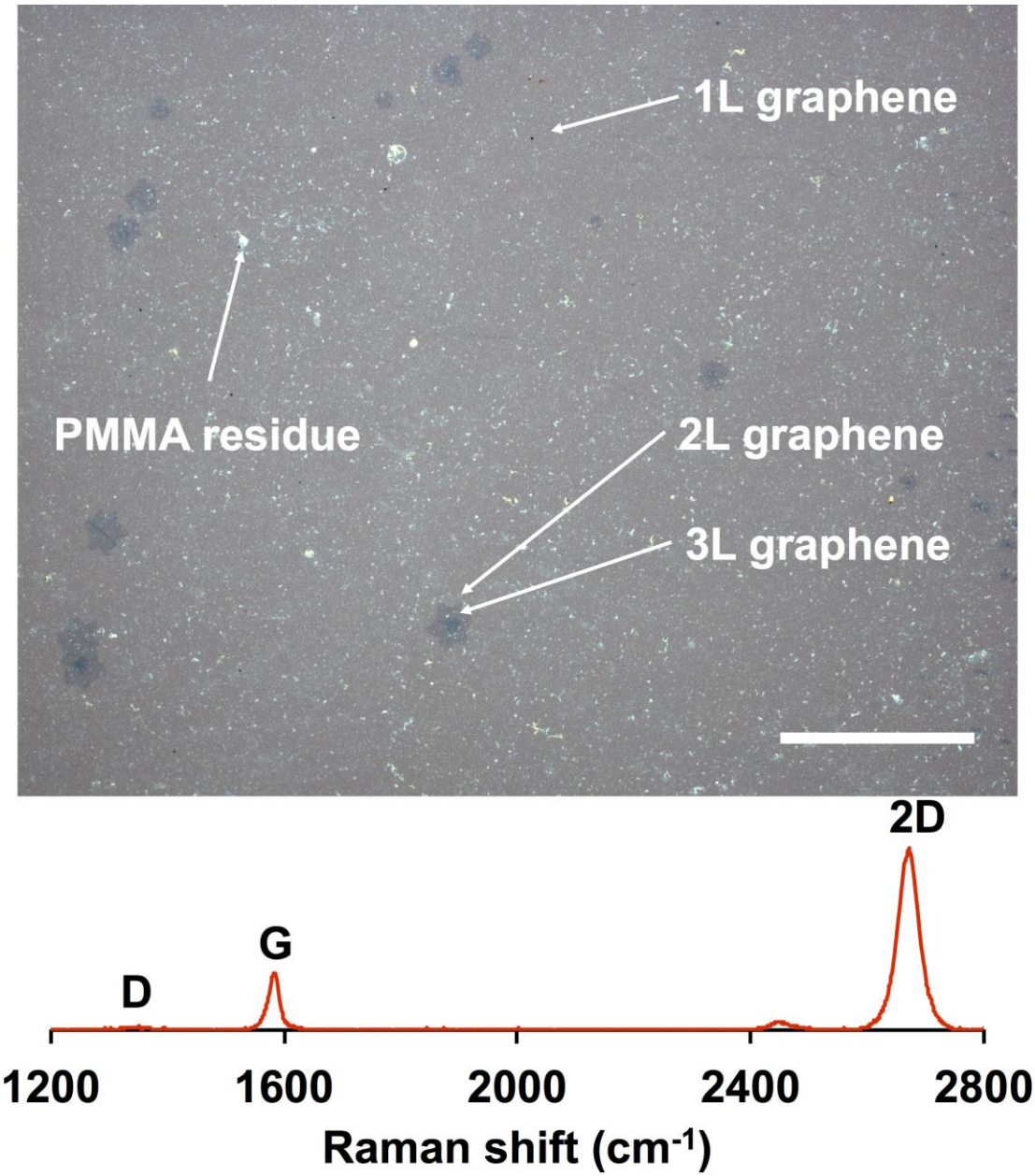


**Figure S1 | Single-layer graphene**. Optical micrograph of single layer CVD graphene wet-transferred to a silicon wafer with 90 nm thermal oxide (top). Scale bar: 100 µm. RAMAN spectrum of single layer CVD graphene wet-transferred to a silicon wafer with 90 nm thermal oxide (bottom). The ratii of the prominent graphene peaks indicate high-quality, predominantly single-layer graphene (D/G ratio: 0.019. 2D/G ratio: 3.1).

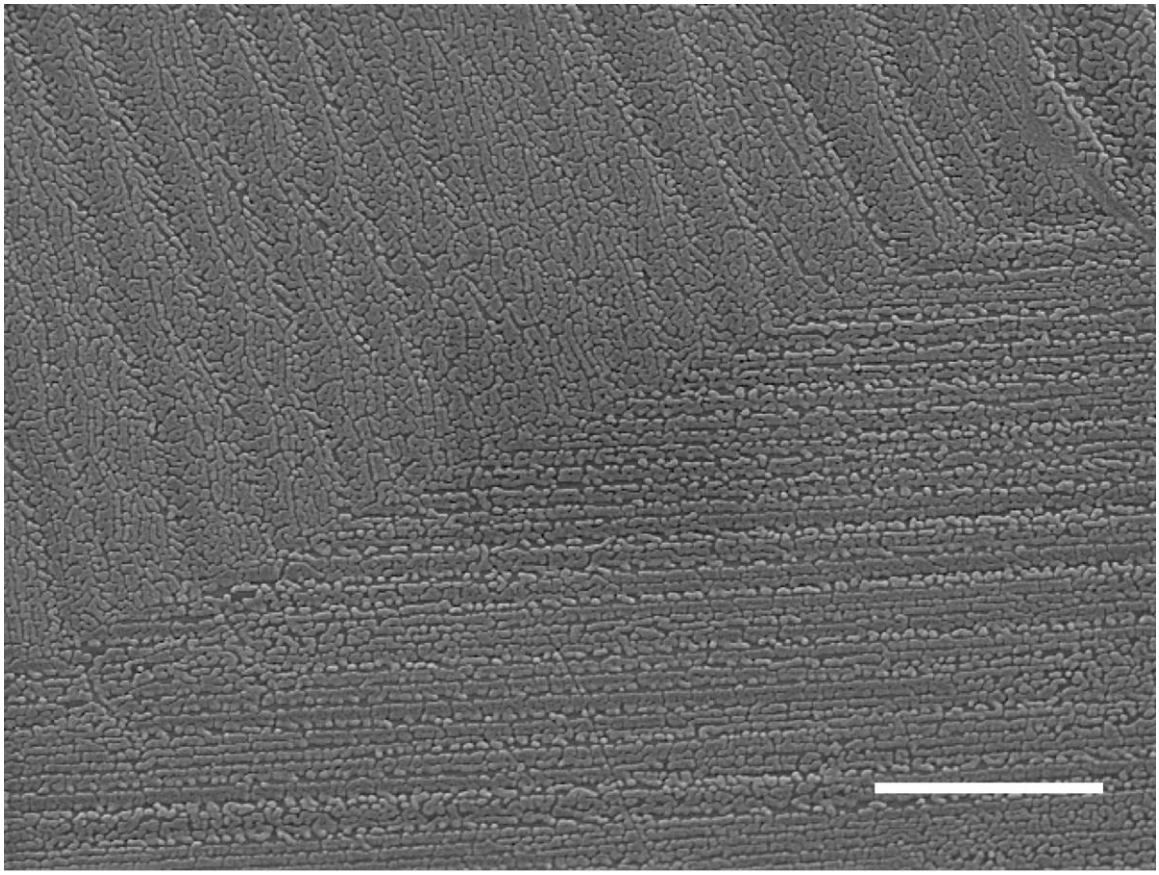

**Figure S2. NI on different substrate grain orientations**. Scanning electron micrograph of AgNI (10 nm deposition) on graphene on copper. Scale bar: 1 µm. Note the copper grain boundary diagonally across the image (from bottom left to top right) and the difference in AgNI morphology (percolation, level of anisotropy) on the respective copper grains.

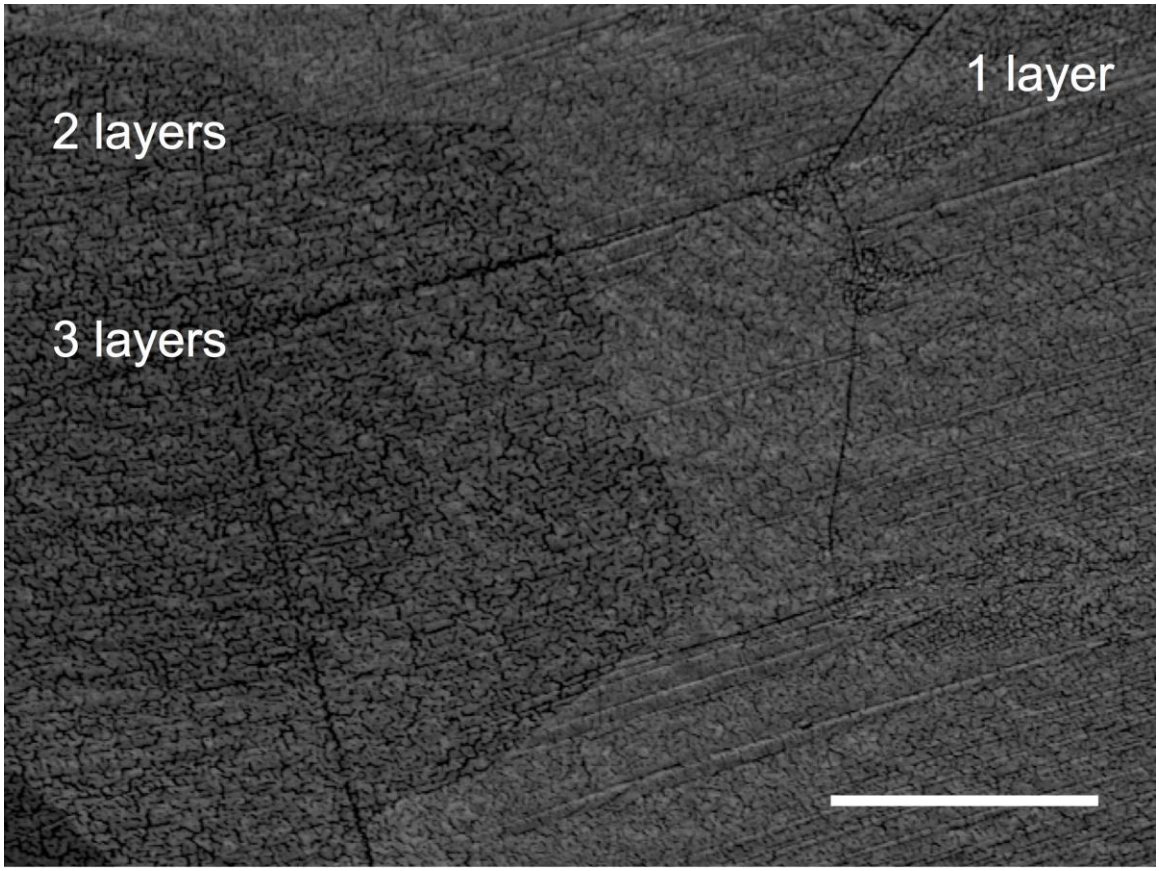


**Figure S3. NI on multiple layers of graphene.** Scanning electron micrograph of AuNI (10 nm deposition onto graphene on copper) on graphene transferred onto Parylene-C (etching copper after deposition of 1 μm-thick film of Parylene C (graphene is on top in this image and is covering the gold islands). Note the change in the amount of percolation in gold islands deposited over 1, 2, and 3 layers of graphene on copper. Scale bar: 2 μm.

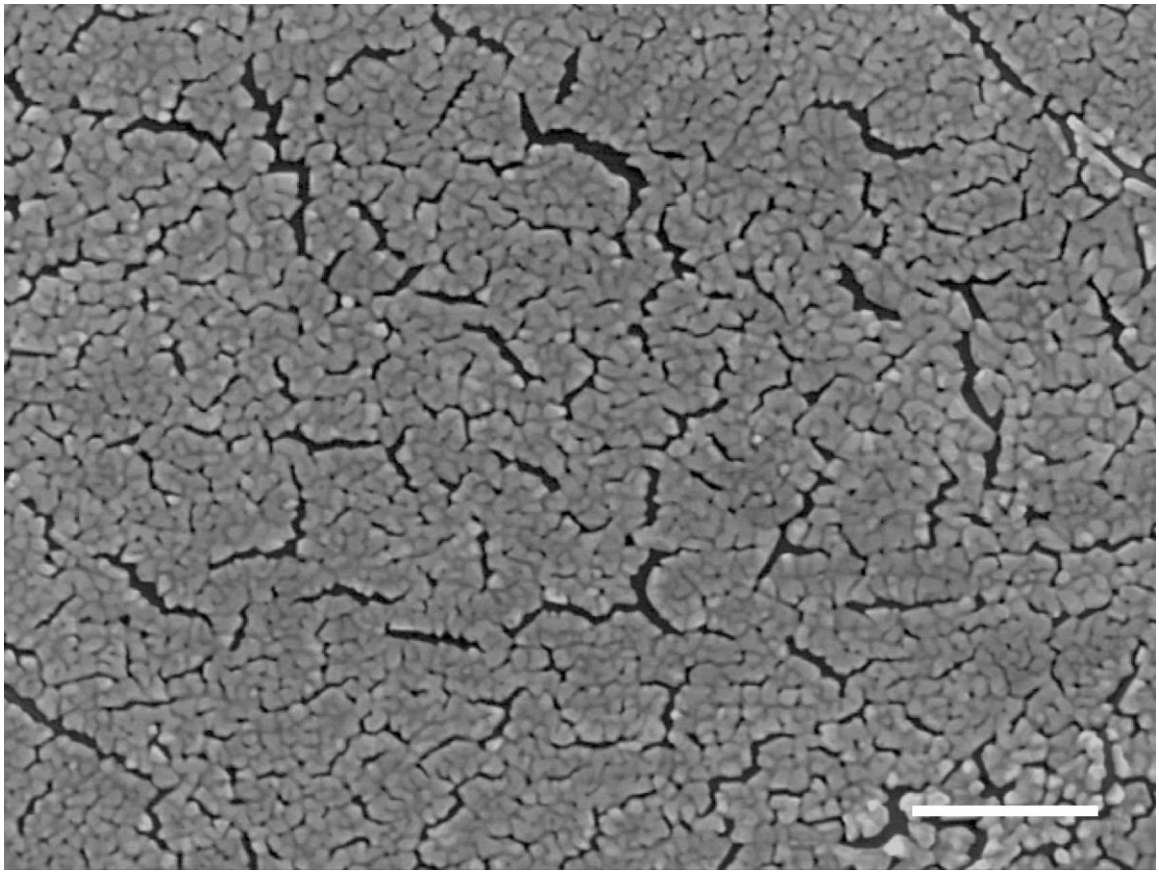

**Figure S4. NI deposited at high evaporation rate.** Scanning electron micrograph of AuNI (10 nm deposition) on graphene on copper deposited at the rate of 2Å/s. Compared to the slow rate of deposition (0.1 Å/s, **Figure 1, bottom**) the structure of the gold islands demonstrates significantly higher granularity, complete percolation, and significantly higher area coverage. Scale bar: 200 nm.

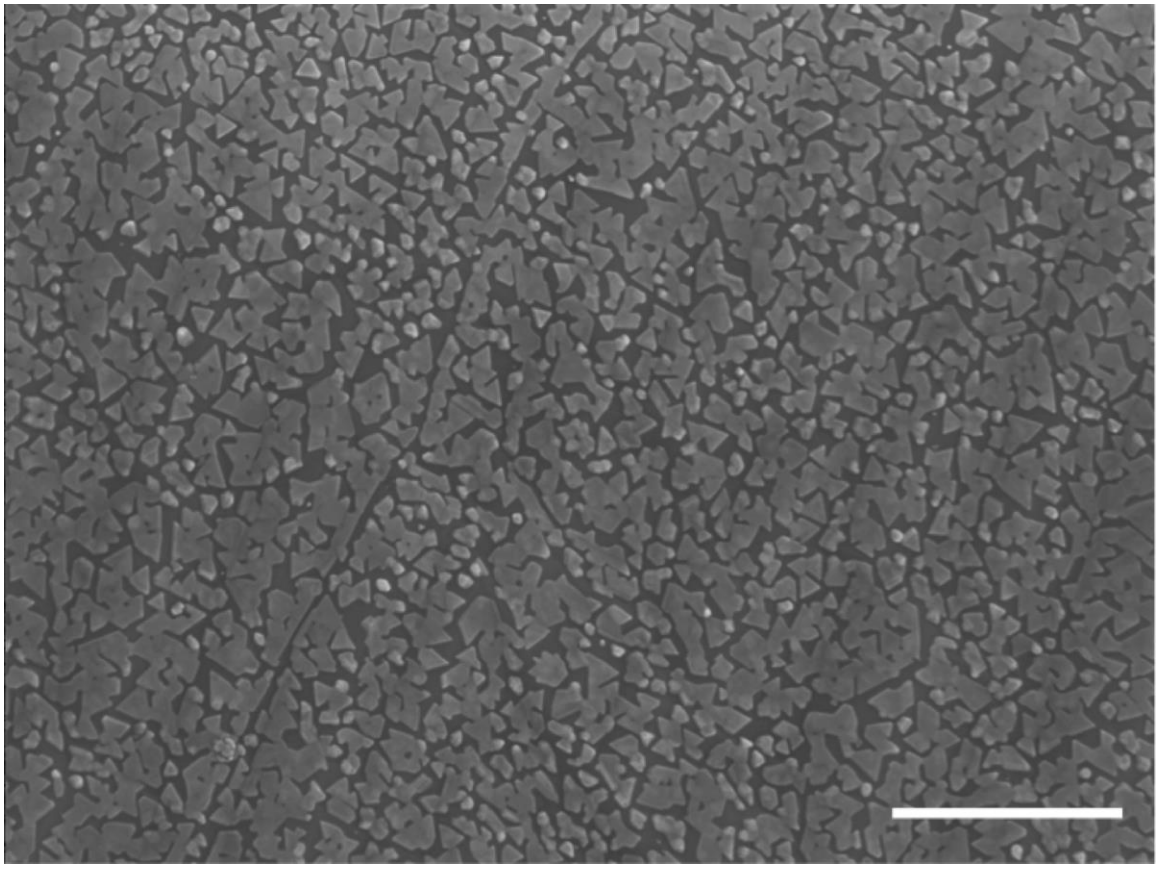

**Figure S5. NI deposited at elevated temperature.** Scanning electron micrograph of AuNI (8 nm deposition) on graphene on copper deposited at the rate of 0.1 Å/s and the substrate temperature ~500 K (100 K higher than SDC used in **Figure 1**). Scale bar: 500 nm.

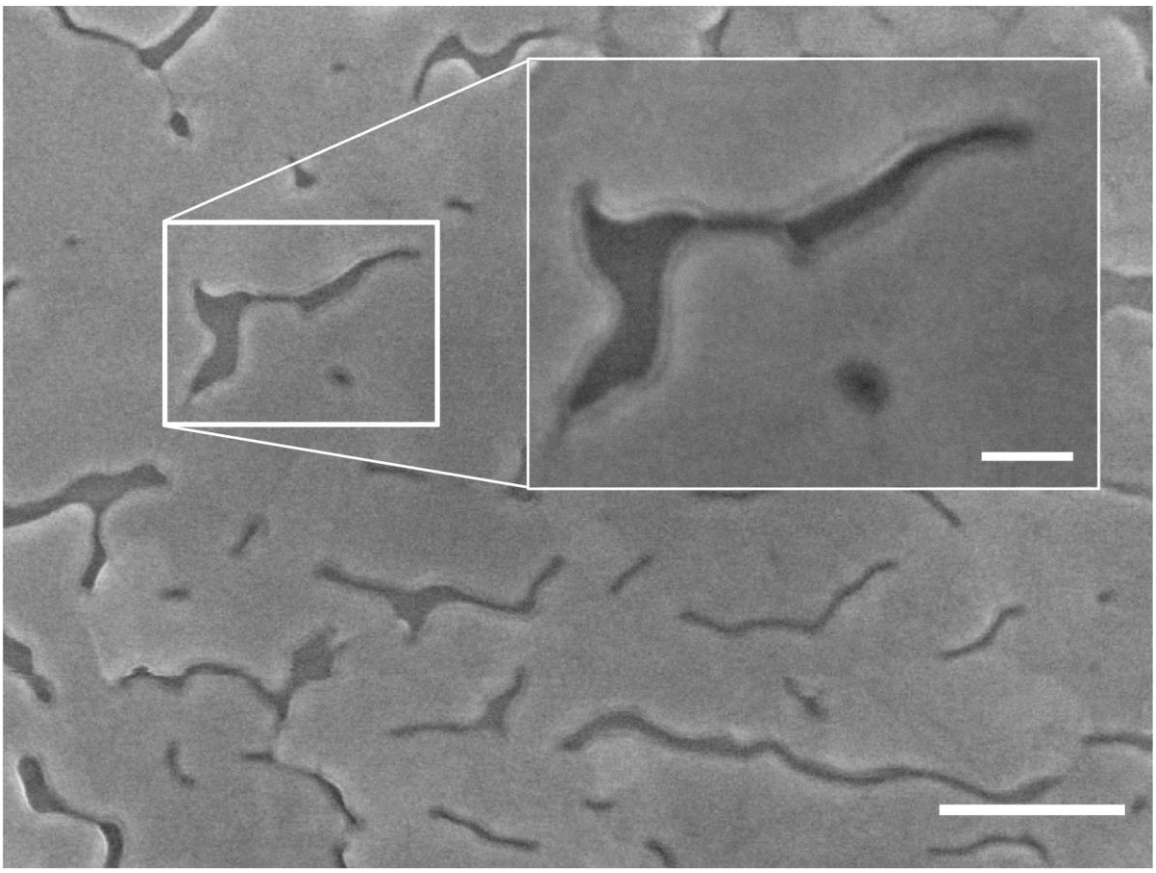

**Figure S6. Thermal annealing of AuNI.** Scanning electron micrograph of AuNI (10nm deposition) on graphene on copper foil after vacuum annealing at 600 K for 1 h. In comparison to the unannealed sample (**Figure 2, top left**), notice merging and spreading of the islands. Scale bar: 200 nm. Scale bar in inset: 50 nm.

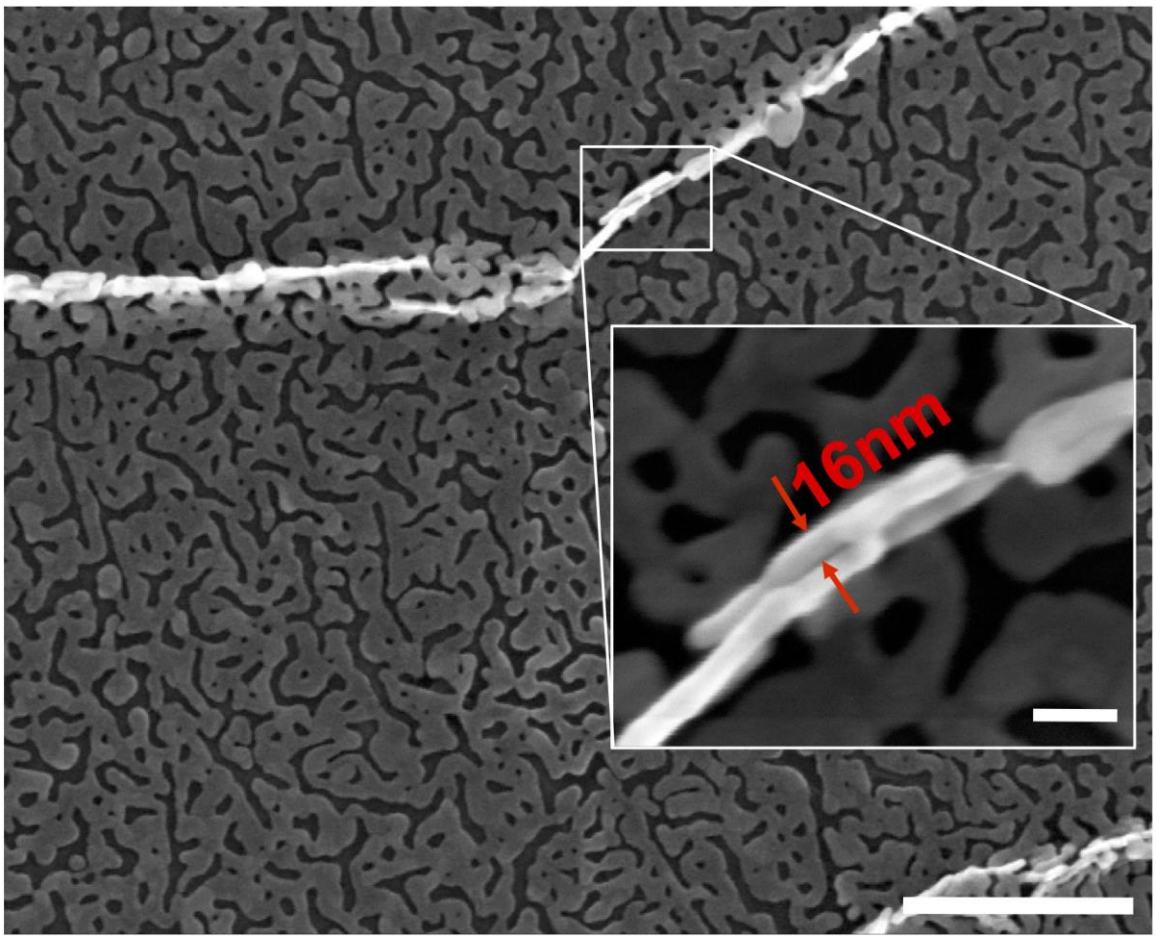


**Figure S7. Wet transfer transforms AuNI.** Scanning electron micrograph of AuNI (10nm deposition) synthesized on graphene on copper foil and transferred onto a glass slide. In comparison to the non-transferred sample (**Figure 1, bottom left**), notice merging of the islands into a completely percolated network and smoothing of the crystal facets. The metamorphosis is potentially due to etching of the copper substrate (surface energy 1650 $mJ/m^2$) away and floating the Au island/graphene film on the surface of water (surface energy 72 $mJ/m^2$) during the wet-transfer process. Notice wrinkles in graphene/AuNI as the result of wet transfer. Scale bar: 200 nm. Scale bar in inset: 50 nm.

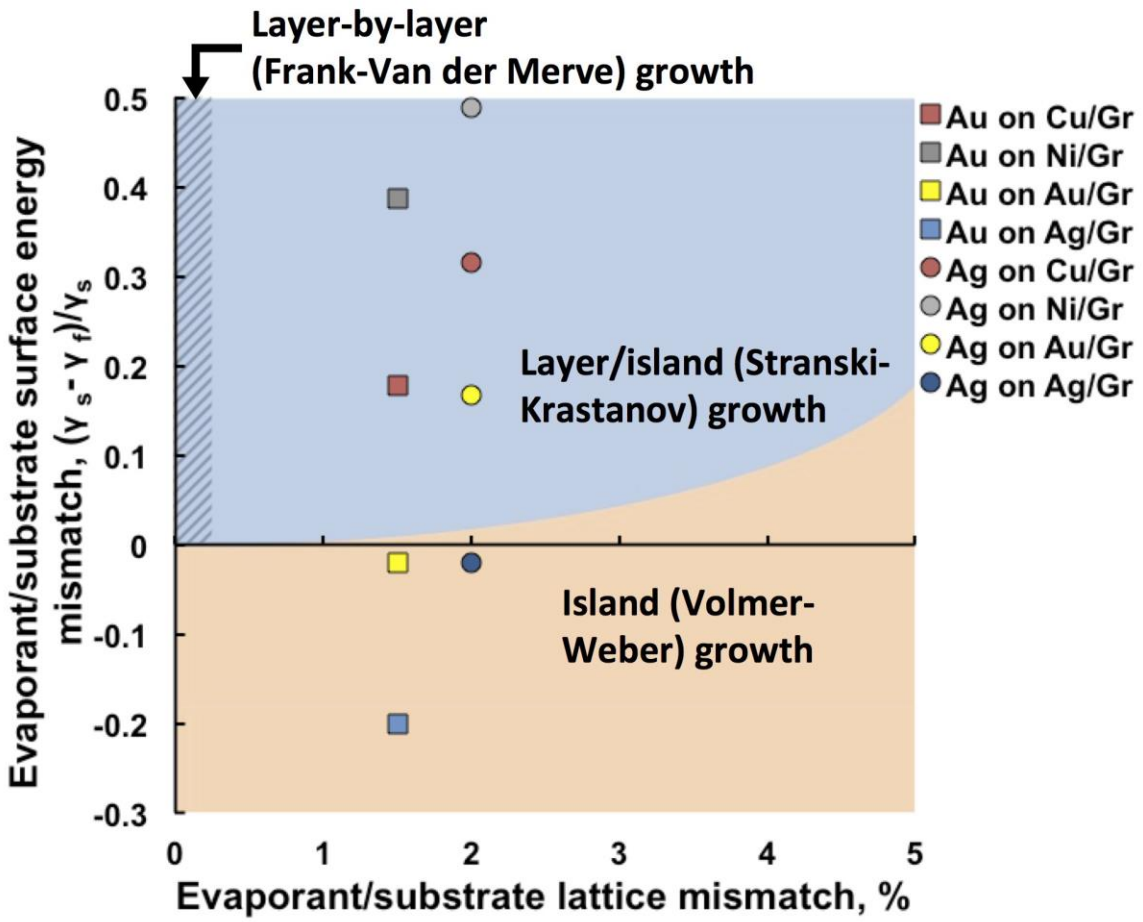


**Figure S8. Thin-film growth model.** Plot of the evaporant/substrate surface energy mismatch (vertical axis) vs. evaporant/substrate (graphene) lattice mismatch (horizontal). Stability regions of the three major modes of film growth are indicated on the plot: layer-by layer (cross-hatch), layer/island (light-blue), island (beige).[23] Note that due to the wetting transparency of graphene, the surface energy of the substrate was calculated as surface energy of the substrate metal less 2% (hence notice the vertical position of same-evaporant/same-metal substrate (Au on Au/Gr and Ag on Ag/Gr) at –0.02. The substrate lattice constant was taken as that of graphene (2.46 Å) (the effect of the strain (≈0.5%)[24] on graphene by the underlying substrates was negligible and not accounted for). This model does not take into account the Moiré patterns (first-order: substrate/graphene and second order: substrate/graphene/evaporant) that can possibly influence the nanoisland morphology. Notice a good accord of the model with the experimental results (**Figure 1, bottom**): higher degree of nanoisland percolation and graphene area coverage suggests the Stranski-Krastanov mode (Cu/Gr, Ni/Gr substrates), while the systems located in the Volmer-Weber stability zone (Ag on Ag/Gr, Au on Ag/Gr, and Au on Au/Gr) clearly have a purely nanoisland morphology.

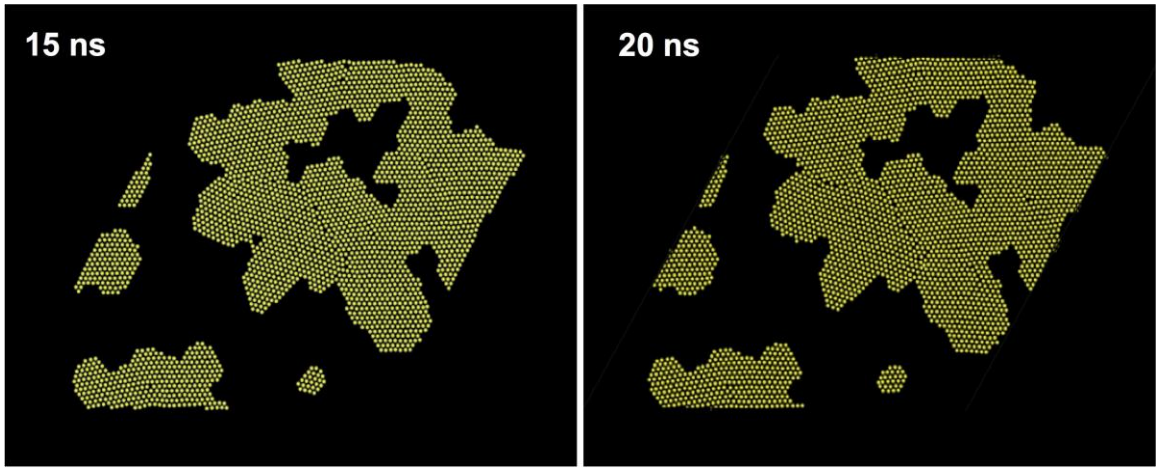


**Figure S9. Monitoring graphene/gold interface events.** LAMMPS simulation of thermal annealing (500°K) of gold nanoislands on graphene on copper. Represented is the reconstruction of the bottom layer of gold (in contact with graphene) over a 5 nanosecond-period during annealing. Notice the reconstruction on the grain boundary between the merged islands and point defect migrations.

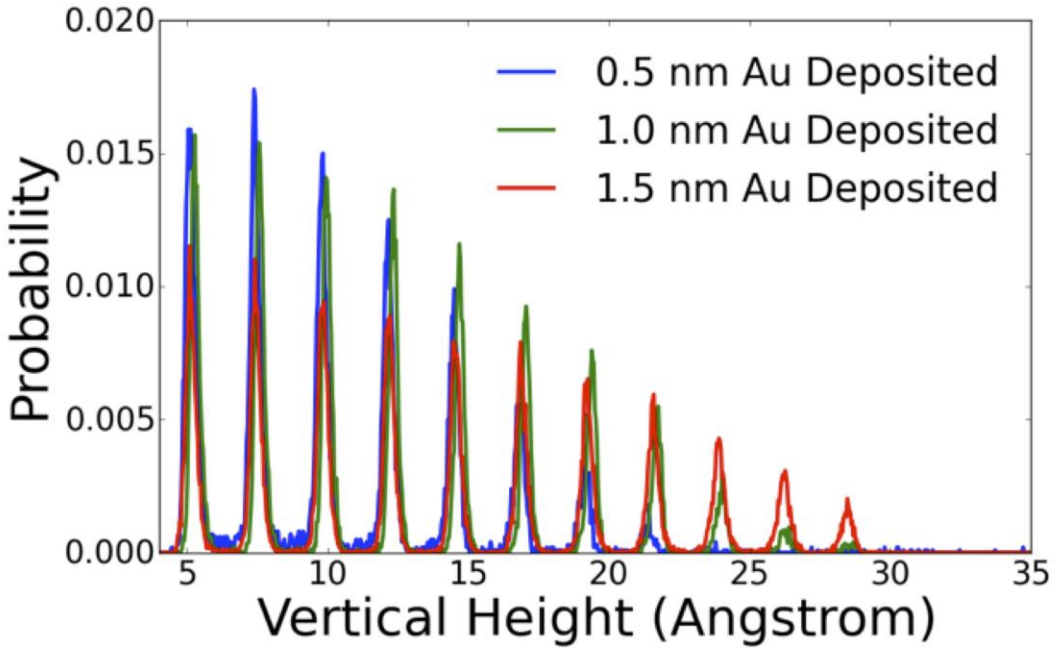


**Figure S10. Monitoring AuNI height distribution during deposition.** Simulated distribution of heights of AuNI (graphene and gold) during the deposition of 2 monolayers of gold.

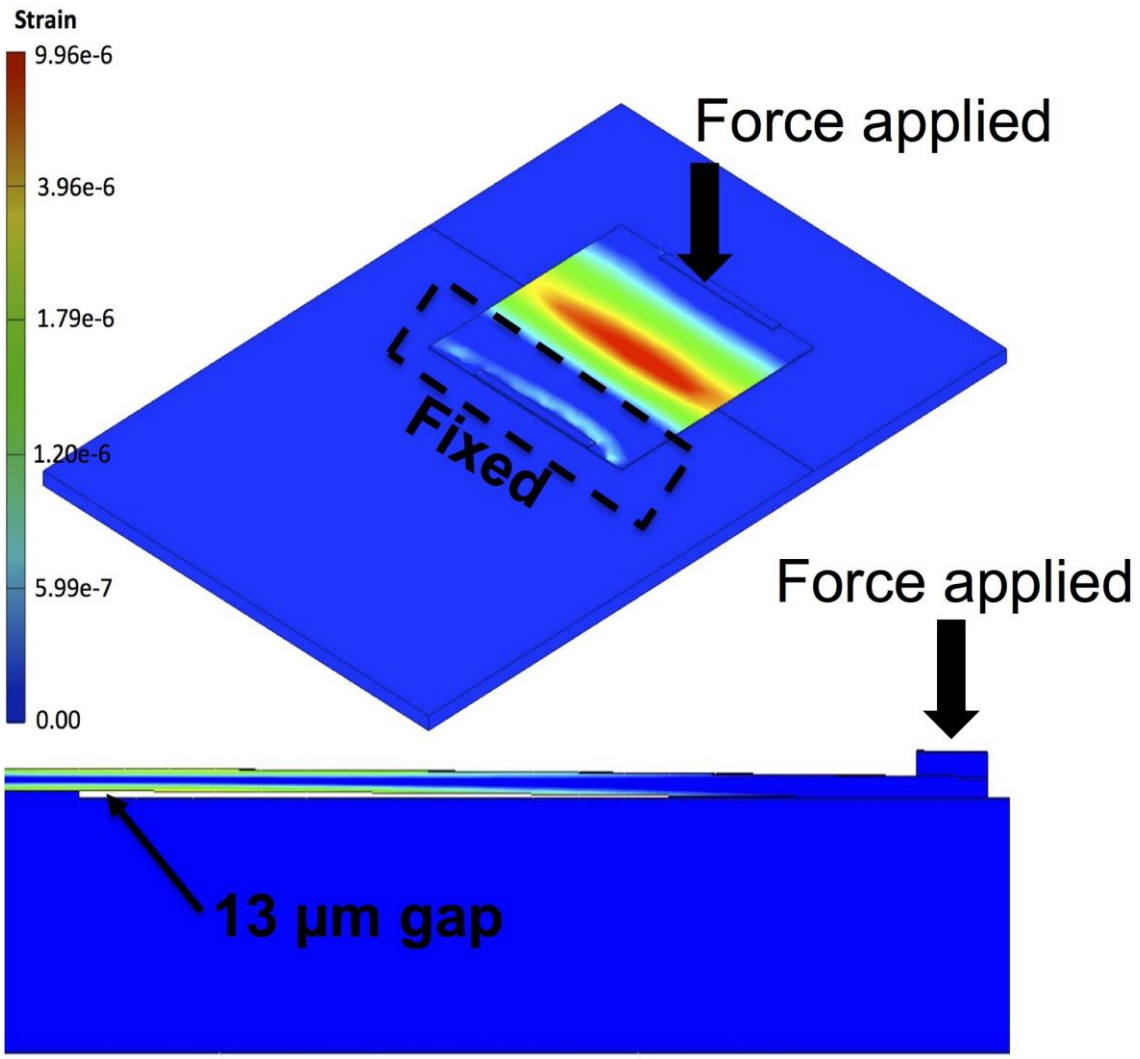


**Figure S11. FEA of glass under small strain**. Finite element analysis simulation of the equivalent strain on the glass cantilever bearing graphene/PdNI strain sensor after applying 0.1N force to the edge of the cantilever. The top surface of the cantilever experiences the maximal tensile strain of 0.001%

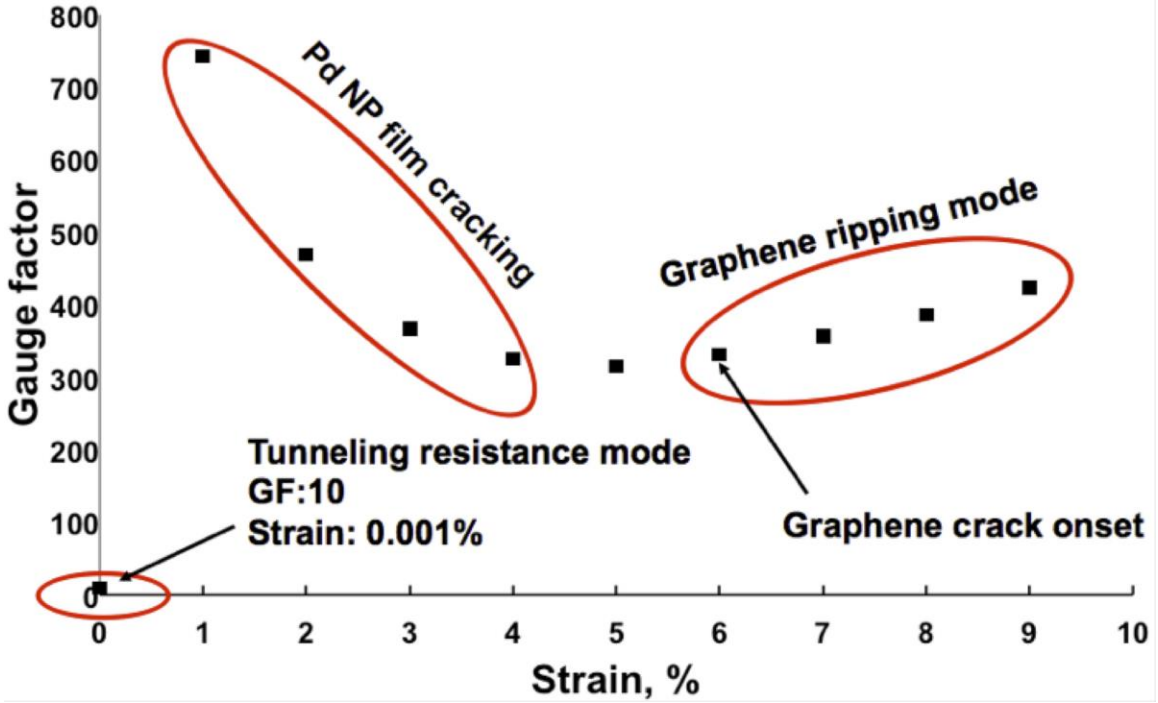


**Figure S12**. **Three sensing modes of graphene/PdNI sensors.** The plot of the gauge factor versus strain % for graphene/PdNI strain sensors indicates three major sensing modes: interparticle tunneling resistance modulation (<<1% strain), PdNI film cracking (<6% strain), and graphene cracking (>6% strain). Note that the lowest value for 0.001% strain was obtained by flexing 130 µm-thick glass slides bearing graphene/PdNI films (**Figure S18a**), while the rest of the values were obtained with sensors transferred to PDMS strips (**Figure S18b**).

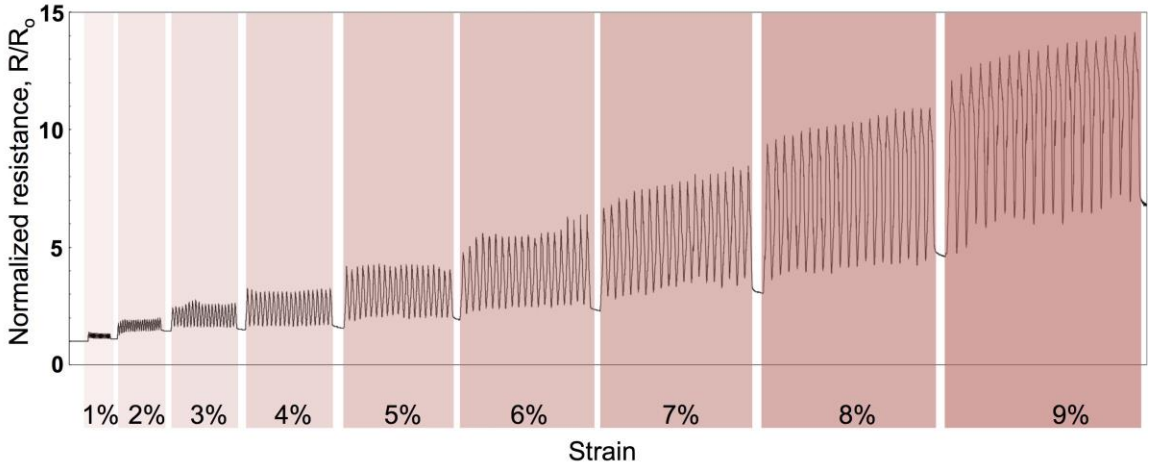


**Figure S13. Graphene as strain sensor.** Normalized resistance plot of graphene on PDMS stretched cyclically (20 cycles for each strain) to 1, 2, 3, … 9% strain. Notice that the baseline within a set of 20 strain cycles is stable until 6% strain is reached (graphene crack onset). The step-wise baseline shift between the sets of different cycles is due to the viscoelastic response of the PDMS substrate.

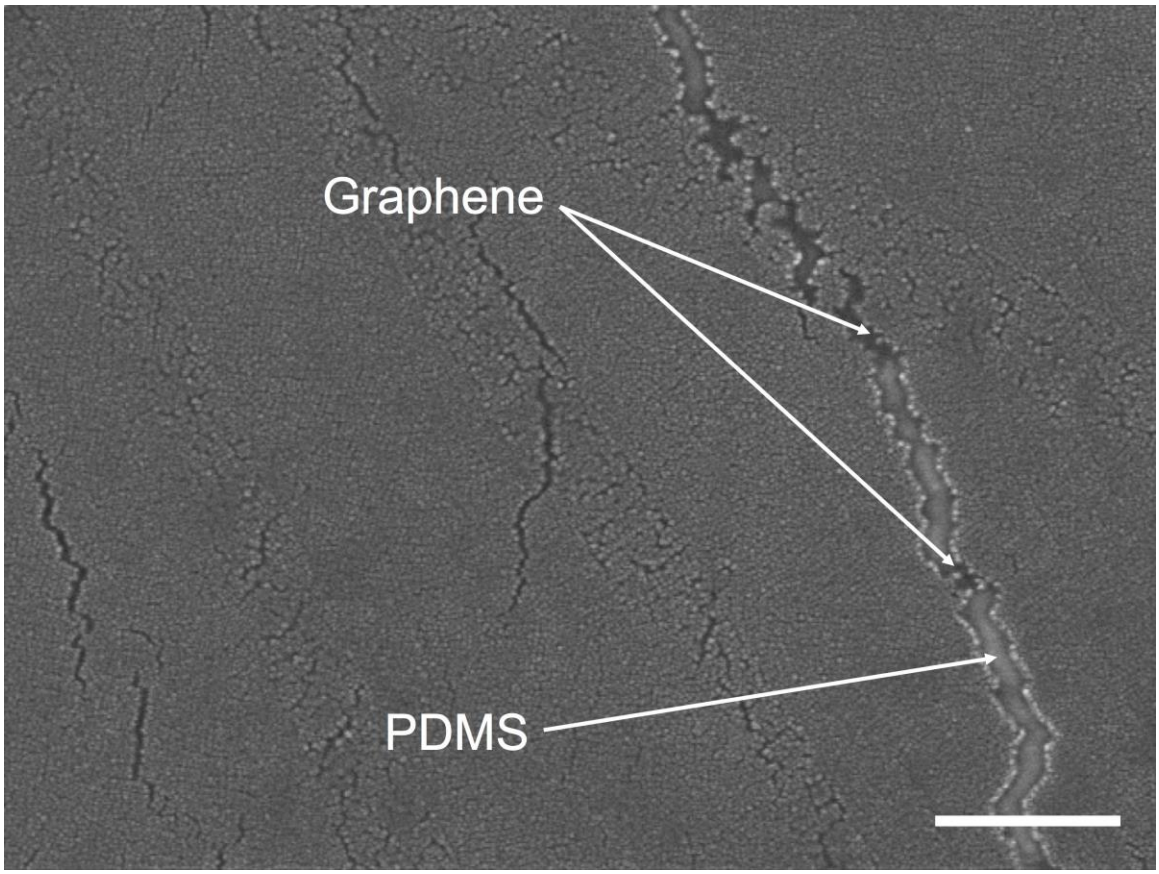


**Figure S14. Graphene/PdNI sensor under 5% srtain.** Scanning electron micrograph of the PDMS/graphene/PdNI strain sensor under tensile strain of ~5% (h). Scale bar: 200 nm.

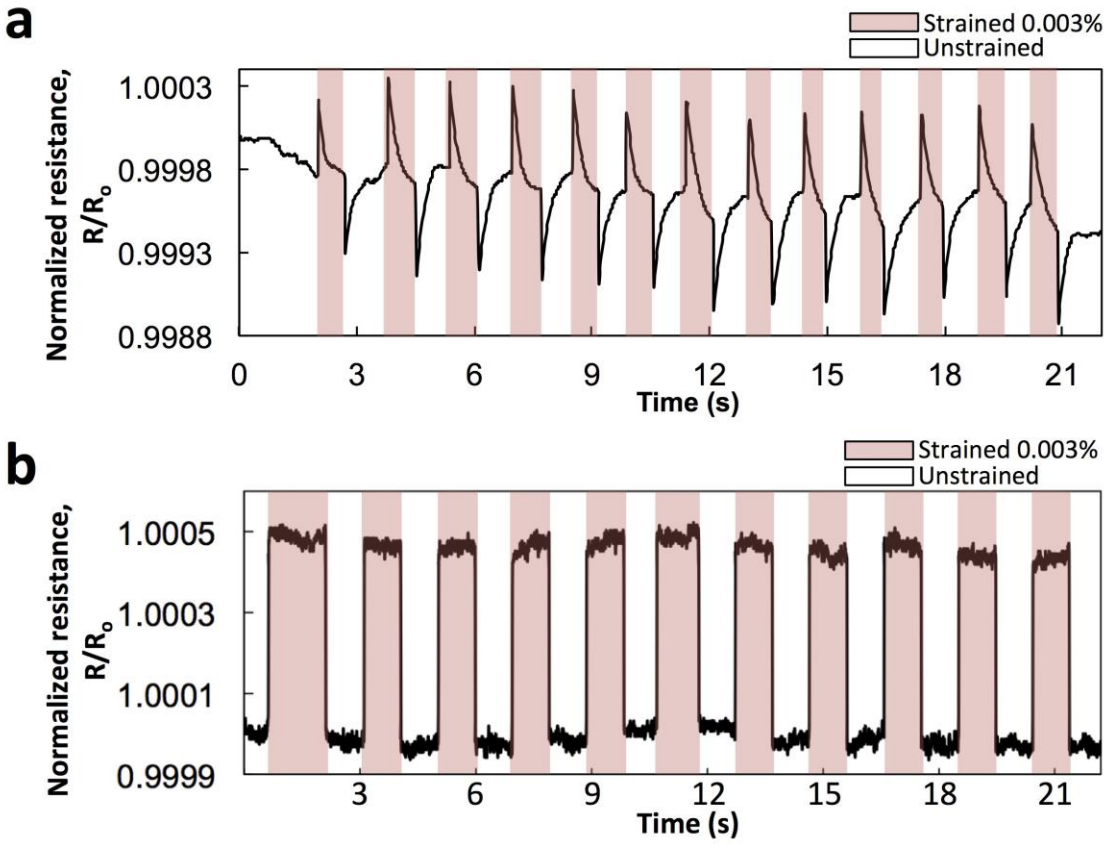


**Figure S15. Solid Pd thin film sensor vs. graphene/PdNI sensor.** Normalized resistance plots of solid (100 nm) film Pd strain sensor on glass coverslip under cyclic tensile strain of 0.003% (a) and the graphene/PdNI strain sensor on glass coverslip under cyclic tensile strain of 0.003% (b). Notice that at similar gauge factors (~17) at 0.003%, the PdNI sensor demonstrates stable behavior (holds the resistance value during the one second strain cycle), while the solid Pd film sensor registers the applied strain but does not hold the resistance value and reverts the it back to the baseline (upon returning the sensor into unstrained position, the resistance value drops and then reverts to the baseline during the one second unstrained cycle). This observation suggests that at very small strains (<<1%), the grain boundaries in the solid Pd film reconstruct to minimize the separation between the grains, which makes impossible to register static strains with such sensors. Conversely, PdNI sensors demonstrate good stability for static strain measurement.

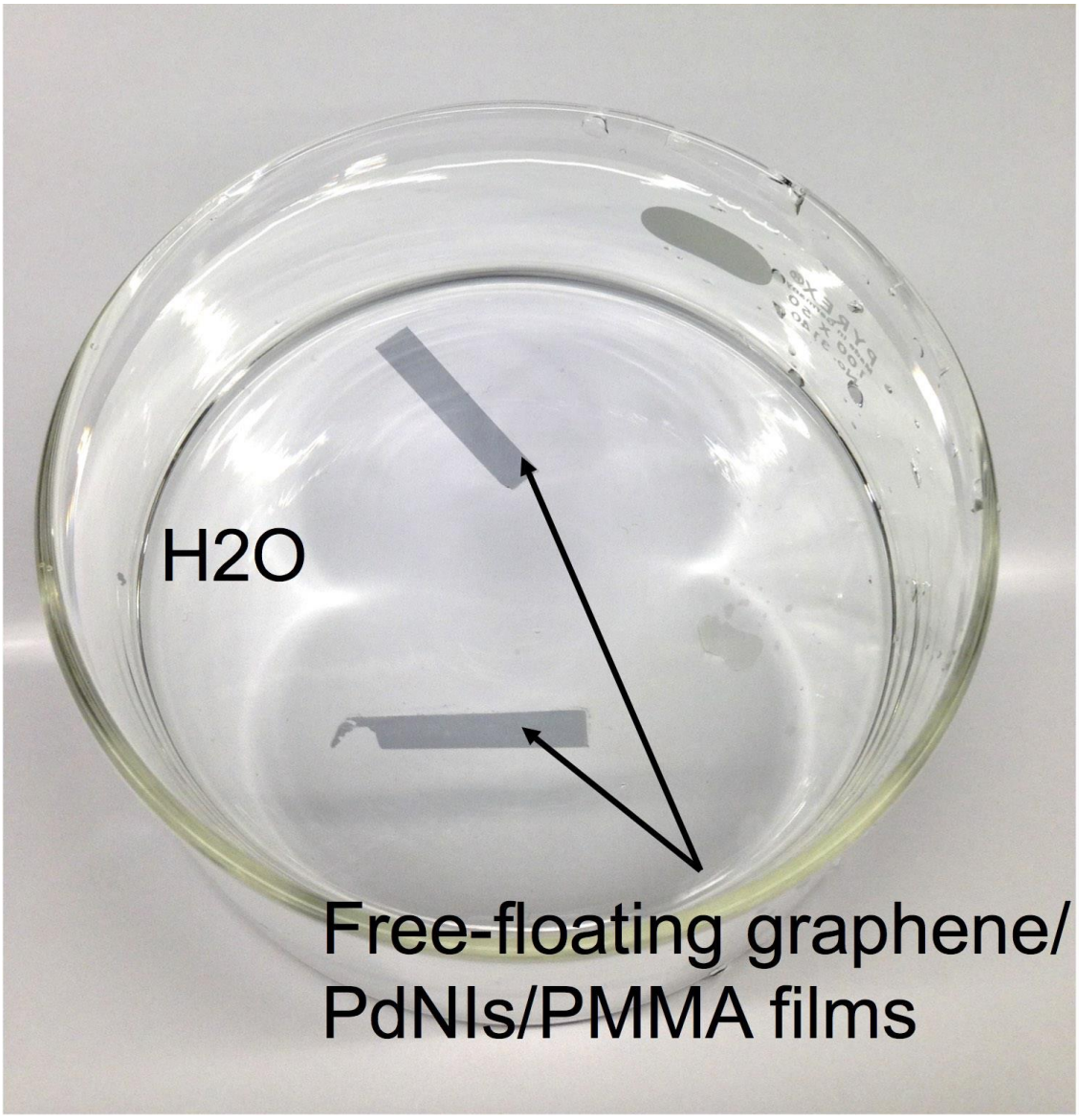


**Figure S16. Free-floating graphene/NI films.** A photograph of free-floating graphene/PdNI/PMMA films after copper etching and transferred into a DI water bath.

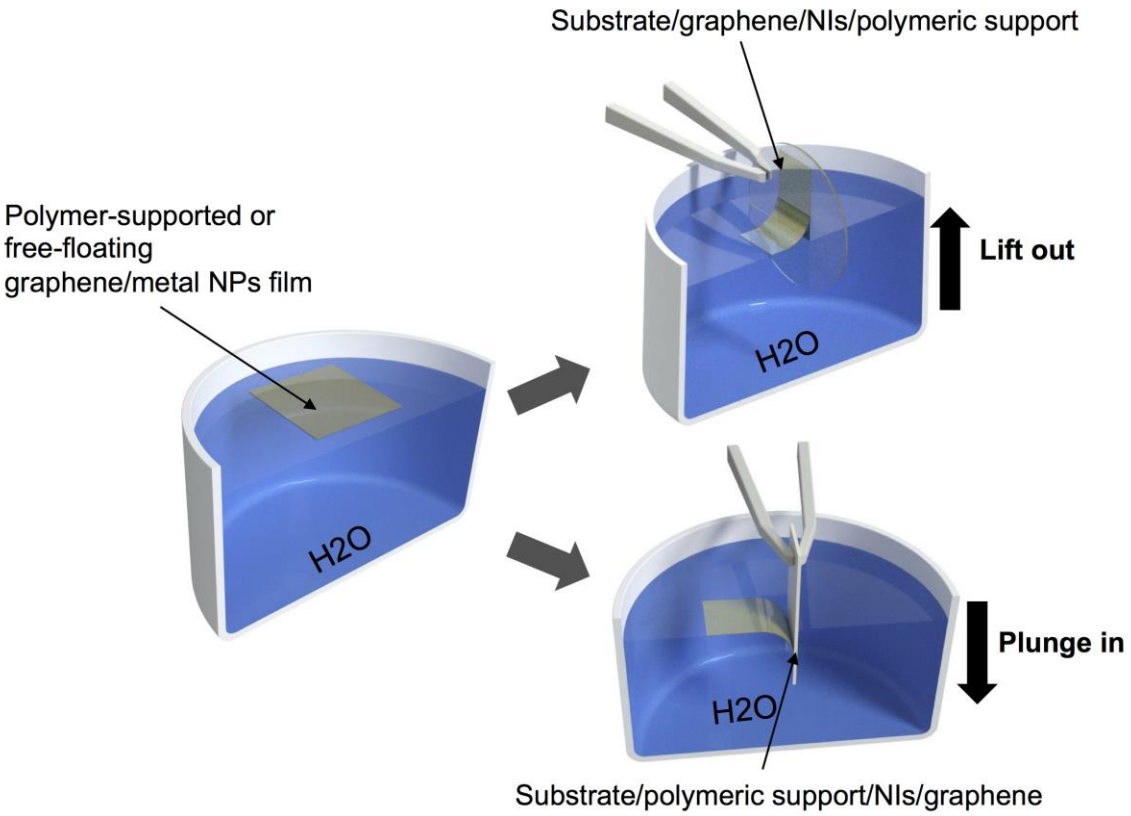


**Figure S17. Graphene/NI transfer.** Rendered schematic of depositing free-floating graphene/NI/polymeric support (or no polymer) onto the final receiving substrate.

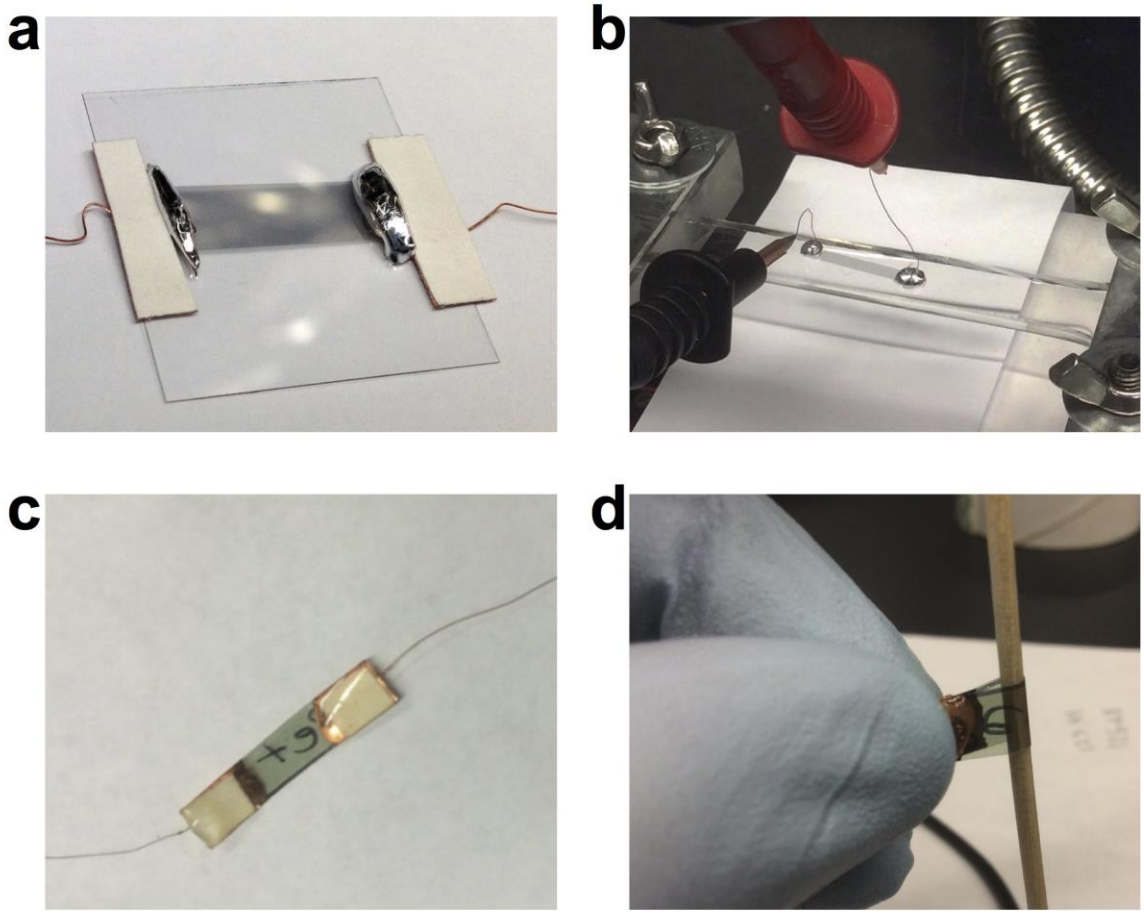


**Figure S18. Graphene/PdNI sensors of rigid, flexible, and stretchable substrates.** Optical photographs of a graphene/PdNI film transferred onto a glass coverslip and electrically addressed with EGaIN and copper wires (a), graphene/PdNI film transferred onto a strip of PDMS under tensile strain cyclic loading (b), PET/PdNI/graphene strain sensors unstrained (c) and bent around a toothpick (d) under ~1% tensile strain.

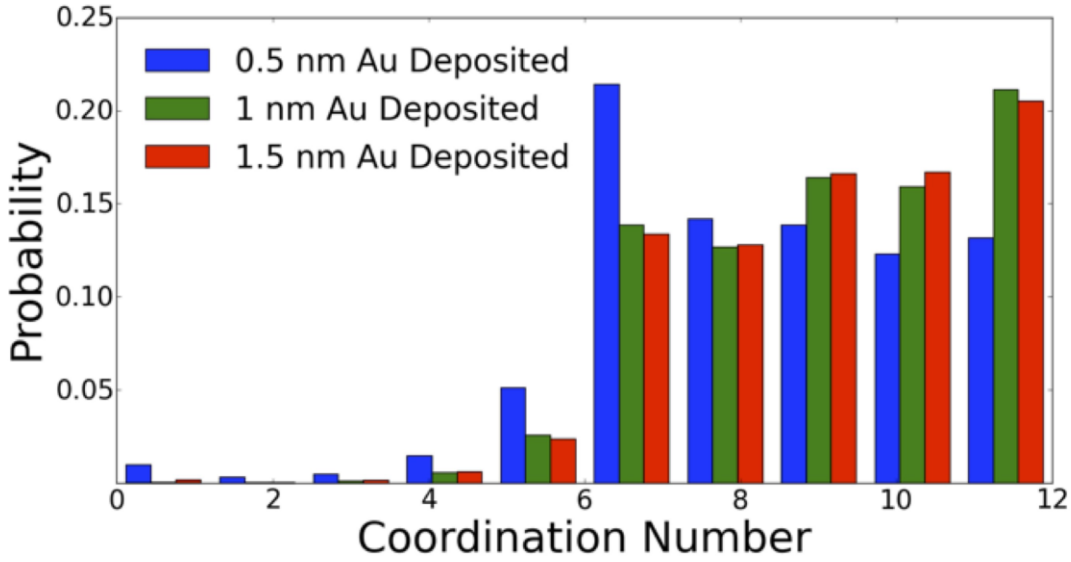


**Figure S19.** Evolution of the coordination number probability distribution as the gold islands are deposited

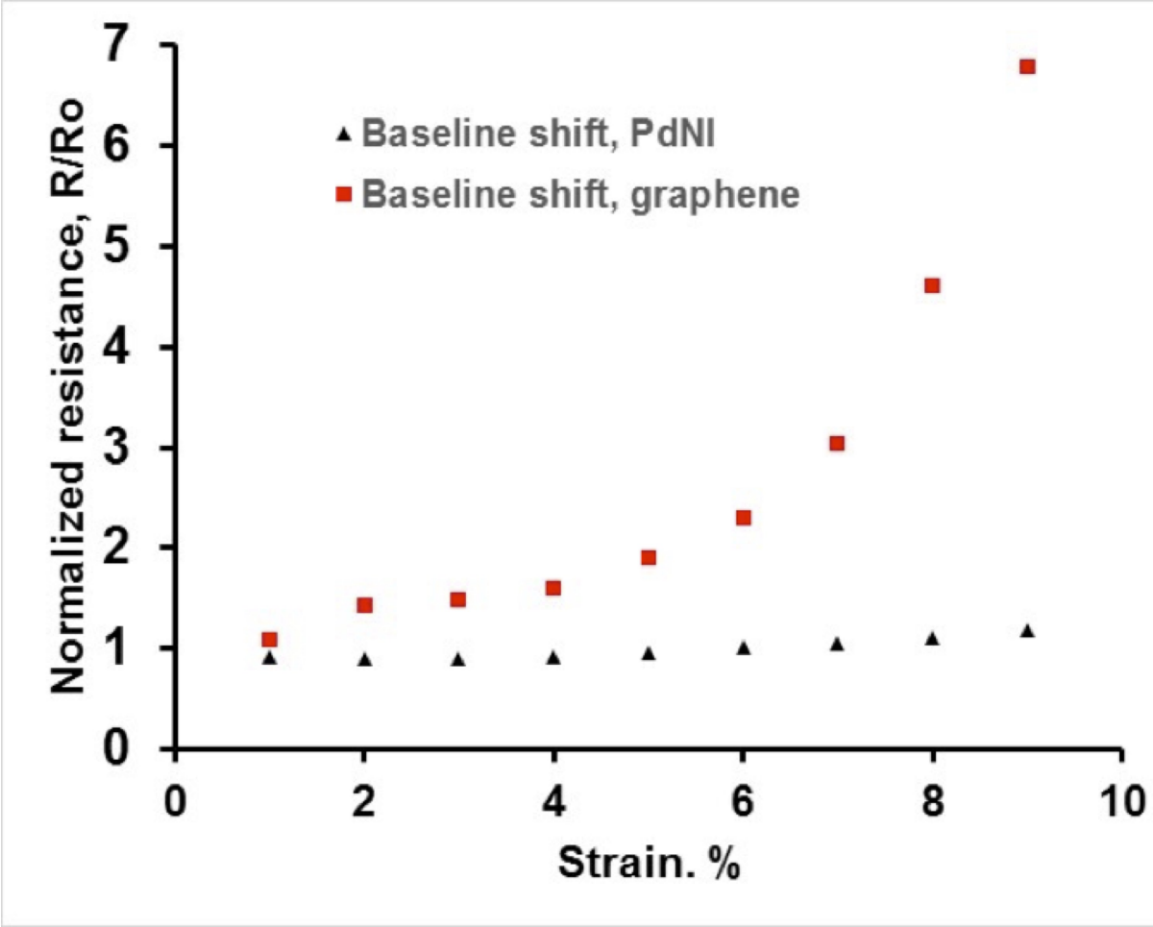


**Figure S20. Sensor baseline stability.** Plot of the baseline shift (normalized resistance) after 1% strain increments (20 cycles per increment) for PdNI sensor on PDMS (black triangles) and graphene on PDMS (red squares). Notice the stability of the PdNI sensor (the baseline normalized resistance drops by 0.11 until 3-4% strain is reached, potentially due to Pd particle repacking; after which it rises minimally to 1.18 after 9% strain cycles). The baseline of the graphene control was rising steadily until 5-6% was reached (graphene crack onset), after which the baseline rose exponentially and reached 6.80 after 9% strain cycles. This indicates that cracks in PdNI films can effectively reclose thus ensuring the stability of the sensor at high strains.

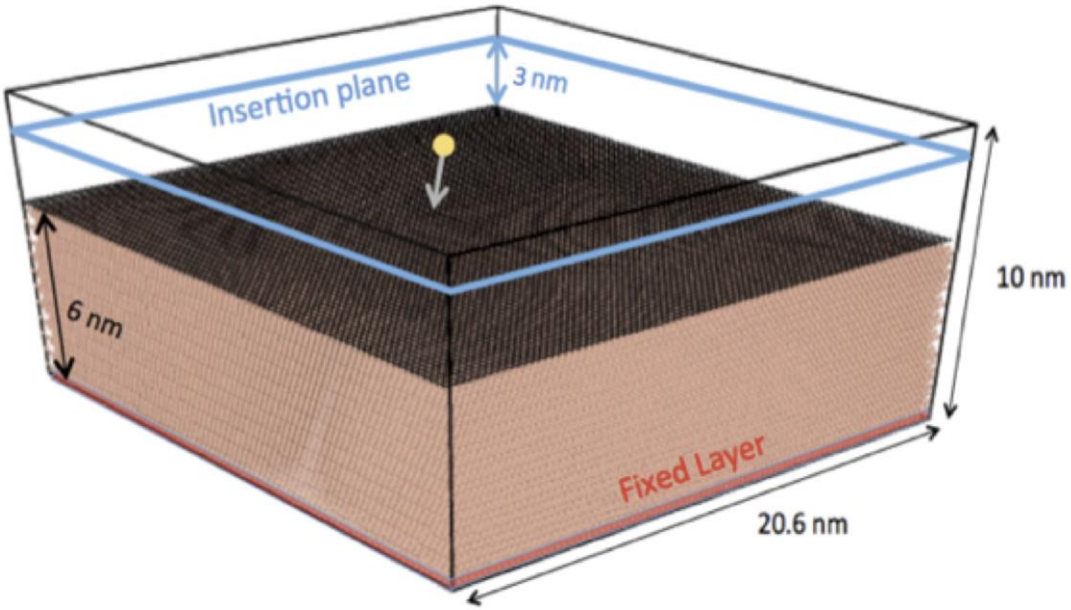


**Figure S21. Simulation box.** Schematic showing the geometry of the graphene/copper substrate.

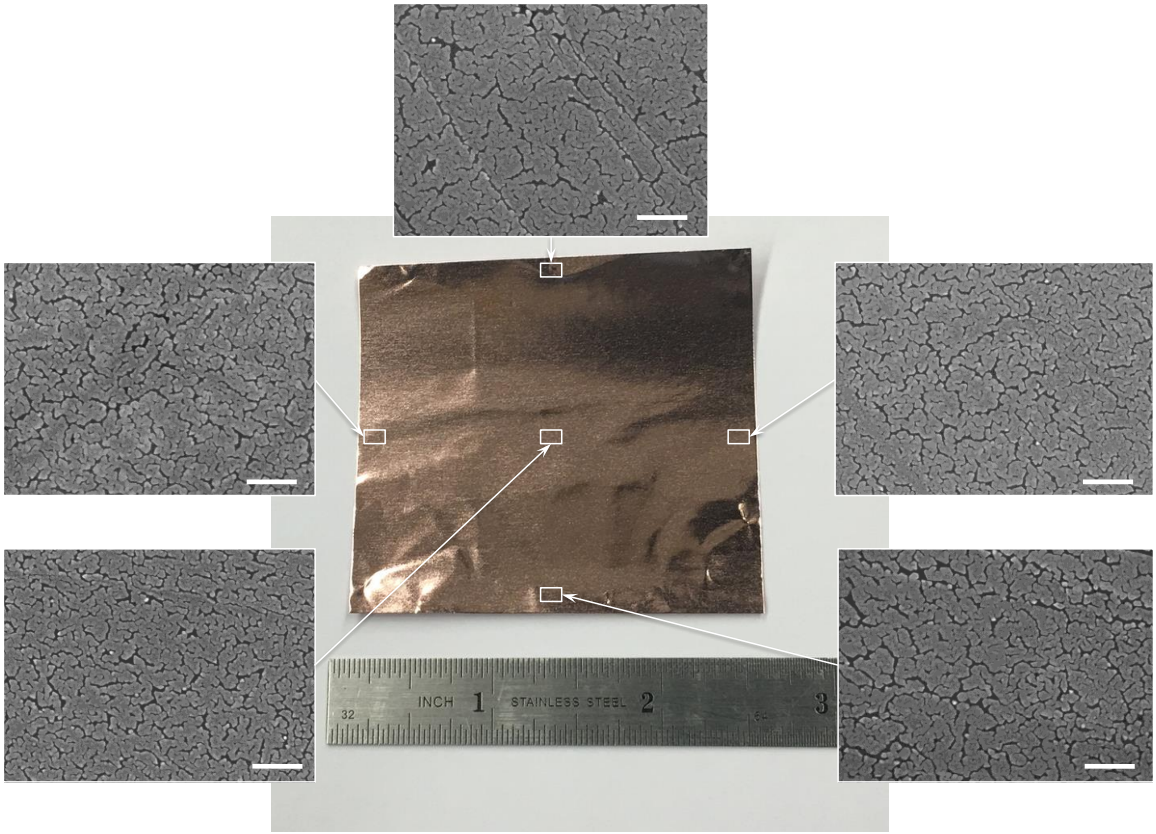


**Figure S22. AuNI uniformity over large area.** Photograph of large-area graphene on copper after the deposition of 10 nm of gold. Insets: SEM images of the corresponding sites throughout the sample. Note the similarity of the NI morphology over ~40 $cm^2$ area. Scale bars: 200 nm.

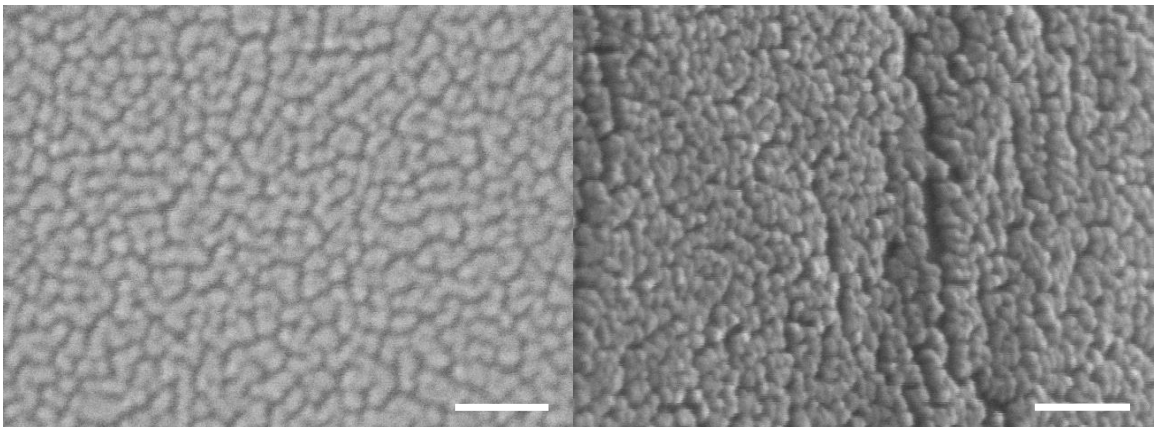

**Figure S23. Coalesced PdNI.** Examples of PdNI films where nanospheres coalesce/aggregate into short chains. Scale bars: 50 nm.

| Interaction Pair | Interatomic Potential |
|---|---|
| Carbon-Carbon | AIREBO [20] |
| Carbon-Copper | Abel-Tersoff Potential [13] |
| Carbon-Gold | Lennard-Jones [22] |
| Copper-Copper | Embedded Atom Method [25] |
| Copper-Gold | Embedded Atom Method [26] |
| Gold-Gold | Embedded Atom Method [19] |

**Table S1.** Summary of interatomic potentials used in this study.

| Sensor geometry | Applied strain range (%) | Range of gauge factor | Range of reproducible behavior (strain, %) | Manipulability* | Biocompatibility | References |
|---|---|---|---|---|---|---|
| Graphene/NI on glass or PDMS | 0.001-9 | 10-1330 | 0.001-9 | YES | YES | This work |
| Colloidal Au NPs on PET | 0.01-0.8 | 59-135 | N/A | No | N/A | Farcau *et al.*[27] |
| Colloidal Au NPs on PET | 0.1-0.6 | 12-190 | 0.1-0.5 | No | N/A | Sangeetha *et al.*[28] |
| Pt NPs sputtered on $SiO_2$ | 0.06-0.15 | 337-735 | N/A | No | N/A | Tanner *et al.*[29,30] |
| PU-PEDOT:PSS/CNT composite | 1.6-100 | <62 | 1.6-3.6 | YES | N/A | Roh *et al.*[31] |

**Table S2. Comparison of graphene/NI strain sensor performance.**
*Manipulability – ability to be transferred onto arbitrary substrates

## References


(1) Vlassiouk, I.; Fulvio, P.; Meyer, H.; Lavrik, N.; Dai, S.; Datskos, P.; Smirnov, S. *Carbon N. Y.* **2013**, *54*, 58–67.

(2) Zhang, B.; Lee, W. H.; Piner, R.; Kholmanov, I.; Wu, Y.; Li, H.; Ji, H.; Ruoff, R. S. *ACS Nano* **2012**, *6*, 2471–2476.

(3) Regmi, M.; Chisholm, M. F.; Eres, G. *Carbon N. Y.* **2012**, *50*, 134–141.

(4) Zaretski, A. V; Moetazedi, H.; Kong, C.; Sawyer, E. J.; Savagatrup, S.; Valle, E.; O'Connor, T. F.; Printz, A. D.; Lipomi, D. J. *Nanotechnology* **2015**, *26*, 45301.

(5) Ohring, M. *Materials Science of Thin Films*; 2001.

(6) Rafiee, J.; Mi, X.; Gullapalli, H.; Thomas, A. V.; Yavari, F.; Shi, Y.; Ajayan, P. M.; Koratkar, N. A. Wetting transparency of graphene. *Nature Materials*, 2012, *11*, 217–222.

(7) Li, X.; Zhu, Y.; Cai, W.; Borysiak, M.; Han, B.; Chen, D.; Piner, R. D.; Colomba, L.; Ruoff, R. S. *Nano Lett.* **2009**, *9*, 4359–4363.

(8) Bae, S.; Kim, H.; Lee, Y.; Xu, X.; Park, J.-S.; Zheng, Y.; Balakrishnan, J.; Lei, T.; Kim, H. R.; Song, Y. Il; Kim, Y.-J.; Kim, K. S.; Ozyilmaz, B.; Ahn, J.-H.; Hong, B. H.; Iijima, S. *Nat. Nanotechnol.* **2010**, *5*, 574–578.

(9) Plimpton, S. *J. Comput. Phys.* **1995**, *117*, 1–42.

(10) Stukowski, A. *Model. Simul. Mater. Sci. Eng.* **2009**, *18*, 015012.

(11) Süle, P.; Szendrő, M. *Model. Simul. Mater. Sci. Eng.* **2015**, *23*, 025001.

(12) Hermann, K. *J. Phys. Condens. Matter* **2012**, *24*, 314210.

(13) Süle, P.; Szendró, M.; Hwang, C.; Tapasztó, L. *Carbon N. Y.* **2014**, *77*, 1082–1089.

(14) Cao, Y.; Zhang, J.; Sun, T.; Yan, Y.; Yu, F. *Appl. Surf. Sci.* **2010**, *256*, 5993–5997.

(15) Zhang, J.; Liu, C.; Shu, Y.; Fan, J. *Appl. Surf. Sci.* **2012**, *261*, 690–696.

(16) Shinoda, W.; Shiga, M.; Mikami, M. *Phys. Rev. B - Condens. Matter Mater. Phys.* **2004**, *69*, 16–18.

(17) Tuckerman, M. E.; Alejandre, J.; López-Rendón, R.; Jochim, A. L.; Martyna, G. J. *J. Phys. A. Math. Gen.* **2006**, *39*, 5629–5651.

(18) Stukowski, A. *Jom* **2013**, *66*, 399–407.

(19) Foiles, S. M.; Baskes, M. I.; Daw, M. S. *Phys. Rev. B* **1986**, *33*, 7983–7991.

(20) Stuart, S.; Tutein, A.; Harrison, J. *J. Chem. Phys.* **2000**, *112*, 6472–6486.

(21) Liang, T.; Shin, Y. K.; Cheng, Y.-T.; Yilmaz, D. E.; Vishnu, K. G.; Verners, O.; Zou, C.; Phillpot, S. R.; Sinnott, S. B.; van Duin, A. C. T. *Annu. Rev. Mater. Res.* **2013**, *43*, 109–129.

(22) Helgee, E. E.; Isacsson, A. *Forthcoming* **2015**, 1–4.

(23) Tu, K.; Mayer, J. W.; Feldman, L. C. *Electronic Thin Film Science: For Electrical Engineers and Materials Scientists*; Macmillan, 1992.

(24) He, R.; Zhao, L.; Petrone, N.; Kim, K. S.; Roth, M.; Hone, J.; Kim, P.; Pasupathy, A.; Pinczuk, A. *Nano Lett.* **2012**, *12*, 2408–2413.

(25) Sheng, H. W.; Kramer, M. J.; Cadien, a.; Fujita, T.; Chen, M. W. *Phys. Rev. B - Condens. Matter Mater. Phys.* **2011**, *83*, 1–20.

(26) Ward, L.; Agrawal, a; Flores, K. M.; Windl, W. *Model. Simul. Mater. Sci. Eng.* **2012**.

(27) Farcau, C.; Moreira, H.; Viallet, B.; Grisolia, J.; Ciuculescu-Pradines, D.; Amiens, C.; Ressier, L. *J. Phys. Chem. C* **2011**, *115*, 14494–14499.

(28) Sangeetha, N. M.; Decorde, N.; Viallet, B.; Viau, G.; Ressier, L. *J. Phys. Chem. C* **2013**, *117*, 1935–1940.

(29) Tanner, J. L.; Mousadakos, D.; Giannakopoulos, K.; Skotadis, E.; Tsoukalas, D. High strain sensitivity controlled by the surface density of platinum nanoparticles. *Nanotechnology*, 2012, *23*, 285501.

(30) Tanner, J. L.; Mousadakos, D.; Broutas, P.; Chatzandroulis, S.; Raptis, Y. S.; Tsoukalas, D. In *Procedia Engineering*; 2011; Vol. 25, pp. 635–638.

(31) Roh, E.; Hwang, B.-U.; Kim, D.; Kim, B.-Y.; Lee, N.-E. *ACS Nano* **2015**, *9*, 6252–6261.